





Mass enhancement in 3d and s-p perovskites from symmetry breakingZhi Wang , Oleksandr I. Malyi , Xingang Zhao , and Alex Zunger *Renewable and Sustainable Energy Institute, University of Colorado, Boulder, Colorado 80309, USA*

(Received 29 January 2021; accepted 8 February 2021; published 9 April 2021)

In some d -electron oxides, the measured effective mass m_{exptl}^* has long been known to be significantly larger than the model effective mass m_{model}^* deduced from mean-field band theory, i.e., $m_{\text{exptl}}^* = \beta m_{\text{model}}^*$, where $\beta > 1$ is the “mass-enhancement” or “mass-renormalization” factor. Previous applications of density functional theory (DFT), based on a symmetry-restricted structure with the smallest number of possible magnetic, orbital, and structural degrees of freedom, missed such mass enhancement. This fact has been taken as evidence of strong electronic correlation, often described via the symmetry-restricted dynamic mean-field approach of the many-body theory, being the exclusive enabling physics. This paper uses instead a static density functional approach that does not restrict positional or spin degrees of freedom (symmetry-broken structures). This approach analyzes the contributions of different symmetry-broken modalities to mass enhancement for a few nominally highly correlated d -electron perovskites as well as the nominally uncorrelated, closed-shell s - p bonding perovskites. It shows that the energy-lowering symmetry-broken spin effects (e.g., nonzero local moment in the paramagnetic phase) and structural effects (e.g., atomic displacement) as described in mean-field DFT already manifest mass enhancement for both electrons and holes in a range of d -electron perovskites SrVO₃, SrTiO₃, BaTiO₃, and LaMnO₃, as well as p -electron perovskites CsPbI₃ and SrBiO₃, including both metals (SrVO₃) and insulators (the rest). This is revealed only when enlarged unit cells of the same parent global symmetry, which are large enough to allow for symmetry-breaking distortions and concomitant variations in spin order, are explored for their ability to lower the total energy. Positional symmetry breaking that leads to mass enhancement includes octahedral rotation in halide perovskites such as CsPbI₃, Jahn-Teller-like Q_2^+ distortion in LaMnO₃, and bond disproportionation in SrBiO₃, while magnetic symmetry breaking resulting in mass enhancement includes the formation of a distribution of local moments in SrVO₃ that averages to zero in the paramagnetic phase. Not all symmetry breaking leads to significant mass enhancement, e.g., the rather small octahedral rotations in the nearly perfectly cubic SrTiO₃ cause negligible mass enhancement, as do the paraelectric displacements in BaTiO₃. In principle, by ergodicity, the two descriptions, i.e., the symmetry-restricted dynamic approach with a single time-fluctuating magnetic moment and the symmetry-broken mean-field approach with a static distribution of spatially fluctuated local moments, are not mutually exclusive but are a choice of representation and consequently, a choice of computational efficiency. In approximate implementations, the symmetry-broken mean-field approach appears to remove much of what was strong correlation in dynamically correlated symmetry-restricted solutions, leaving smaller (“weak”) residual correlation with respect to the exact solution.

DOI: [10.1103/PhysRevB.103.165110](https://doi.org/10.1103/PhysRevB.103.165110)**I. INTRODUCTION**

The effective mass m^* defined as the reciprocal of the wave vector curvature $\partial^2 E / \hbar^2 \partial k_i \partial k_j$ of the band dispersion relation $E(k)$ (where k_i and k_j are wave vectors) is a central quantity in condensed matter physics, widely used to characterize the band structure, carrier transport, and wave function localization [1]. Recently, this quantity has attracted attention in the context of d -electron correlated oxide physics, where the measured effective mass m_{exptl}^* has been noted in some cases to be significantly larger than the model effective mass m_{model}^* , deduced from simplified mean-field band theory $m_{\text{exptl}}^* = \beta m_{\text{model}}^*$, where β is the “mass-enhancement” or “mass-renormalization” factor. Here, m_{exptl}^* are generally deduced from experiment via model assumptions (such as band parabolicity or various averages over

the mass tensor), leading to different effective mass definitions in different experiments, including the mass deduced from Fermi velocity (v_F) as $m^* \propto 1/v_F$, from density of states (DOS) $m^* \propto [D(E)]^{2/3}$, from specific-heat coefficient $m^* \propto \gamma$, from magnetic susceptibility $\chi \propto m^*(1 - \frac{m_0^2}{3m^{*2}})$, and from the band width $W \propto \frac{1}{m^*}$. Values of $\beta > 1$ were reported in the literature for Fe-based superconductors [2,3], halide perovskites [4], titanites [5–7], ruthenates [8–10], and vanadates [11–14]. These mass enhancement factors from experiment $\beta(\text{exptl}/\text{model}) = m_{\text{exptl}}^*/m_{\text{model}}^*$ were then compared with the theoretical values $\beta(\text{Theory}/\text{model}) = m_{\text{Theory}}^*/m_{\text{model}}^*$ obtained from many-body approaches (such as dynamic mean-field theory (DMFT) [15–24]). Because m_{model}^* comes from the mean-field band theory, the predicted theoretical enhancement $\beta(\text{Theory}/\text{model}) > 1$ has been interpreted to be due to strong correlation effects [15–24]. For example, in DMFT, wavefunction localizes and bandwidth narrows (thus leading to mass enhancement) due to pure electronic symmetry breaking induced by the dynamic

* alex.zunger@gmail.com

self-energy from the impurity atom embedded in a mean-field bath [24,25]. Finding for a compound that $\beta(\text{DMFT}/\text{model}) > 1$ is consistent with $\beta(\text{exptl}/\text{model}) > 1$ helped classify the pertinent compounds as being highly correlated, given that mean-field theory has been argued as unable to describe the mass enhancement.

This line of thinking, however, does not consider the possibility that mass enhancement could be described by methods other than using symmetry-restricted structures. Indeed, the model calculations used to extract m_{model}^* have invariably been rather naïve (N) level of density functional theory (N-DFT), based on symmetry-restricted structures with the least number of possible magnetic, orbital, and structural degrees of freedom [15–24]. Such calculations have assumed one or a few of the following approximations: A highly symmetric unit cell [e.g., $Pm\bar{3}m$ cubic containing only a single formula unit (f.u.)], no atomic displacements relative to the averaged high-symmetry structure, and/or a nonmagnetic (NM) spin configuration. The shortcomings of such simplistic N-DFT approaches are evident among others in (i) predicting metallic states for known insulators (as illustrated for binary $3d$ NiO, MnO, CoO, and FeO insulators [26], ternary $3d$ oxide perovskites LaVO₃, LaMnO₃, and YNiO₃ [27], as well as other compounds such as CaIrO₃, LaTiO₃, SrBiO₃, TiO_{2-x}, CeO_{2-x}, CuBi₂O₄, Sr₂IrO₄, Li_xTiO₂, and Ba₄As₃ [28,29]), and by the fact that (ii) they predict a total energy far higher (by ~ 1 eV/f.u.) than what conventional DFT [27] provides, as well as by (iii) missing the orbital order [27].

The failures of these naïve applications of mean-field band theory to predict electronic properties often go hand in hand with the assumption of a symmetry-restricted structure. For example, the cubic crystal structure of halide perovskites ABX_3 ($A = \text{Cs, MA, FA}$; $B = \text{Sn, Pb}$; $X = \text{Cl, Br, I}$) has been described in x-ray diffraction (XRD) databases as $Pm\bar{3}m$ cubic, having a single ABX_3 f.u., with all octahedra being ideally shaped, untitled, and oriented parallel to each other, representing a single BX_6 local motif (monomorphous structure). This $Pm\bar{3}m$ cubic structure has been extensively used [30–33] to calculate the standard electronic band structure as well as phonon lattice dynamics. However, in reality, the cubic phase of such ABX_3 perovskites often manifests static atomic distortions off Wyckoff positions as an intrinsic expression of their chemical bonding, as seen by local probes [34,35] and reproduced by static total energy optimization [36], even before the contribution of thermal motion sets in. Whereas this symmetry breaking is observable from x-ray local probe measurements, e.g., the extended x-ray-absorption fine-structure (EXAFS) and pair distribution function (PDF) [37–42], it is easy to miss in DFT if one uses the average XRD $Pm\bar{3}m$ cubic cell because such a single cell geometrically excludes the creation of a periodic lattice with tilted octahedra. Permitting a larger cell (“supercell”) with constrained cubic lattice vectors provides the geometrical freedom to distort octahedra. Similarly, there are reasons to suspect that this simpler symmetry-breaking physics, positional as well as magnetic (both sanctioned by single-determinant mean-field band theory view), could also affect the effective mass. For example, oxide perovskites are known to manifest octahedral rotations and tilting [43], displacements [44], bond disproportionation [45], and Jahn-

Teller distortions [46], while such local modes can couple to the electronic structure, leading to shifted band energies [30,47–52], thus, possibly leading to mass renormalization. Also, whereas the paramagnetic (PM) phases in $3d$ oxides were once treated as NM [12–18,53–55] (thus, interpreting the zero global magnetic moment as being zero on an atom-by-atom basis), more recent theories allowed for the existence of a distribution of different spin environments adding up to zero, constituting a polymorphous network that couples to electronic properties [36,56–58]. The existence of a distribution of positional as well as local magnetic environments needs to be investigated for its ability to affect the band structure and hence the effective masses.

Therefore, instead of leapfrogging from N-DFT to dynamically correlated methods such as DMFT, it would seem informative to retain the m_{model}^* mass but replace m_{Theory}^* in $\beta(\text{Theory}/\text{model}) = m_{\text{Theory}}^*/m_{\text{model}}^*$ by mean-field theory, which allows for possible magnetic, orbital, and structural degrees of freedom, which could break symmetries while lowering the total energy. It can be done by using DFT that is free from oversimplified symmetry-restricted approximations which are not an essential part of DFT. This $\beta(\text{DFT}/\text{N-DFT}) = m_{\text{DFT}}^*/m_{\text{N-DFT}}^*$ might include many symmetry-broken effects routinely included in contemporary DFT calculations, such as (i) positional symmetry breaking, e.g., octahedral rotations, Jahn-Teller distortions, and bond disproportionation, all observed experimentally, and (ii) magnetic symmetry breaking, e.g., allowing spin configurations such as antiferromagnetic (AFM) and PM rather than the NM approximation. Effective allowance for (i) and (ii) also necessitates the use of exchange-correlation (XC) functionals that produce correctly compact orbitals (due to closer adherence to the generalized Koopmans condition [59]) but not an overestimated orbital localization (such as in the Hartree-Fock functional).

That symmetry breaking in approximate mean-field theory could capture events that in restricted symmetric structures would require a complex correlated treatment has been amply illustrated in molecular systems. For example, as pointed out by Bagus and Schaefer [60], describing a core hole state in diatomic O₂ while retaining the high $D_{\infty h}$ symmetry is made computationally difficult by the extreme complexity of packing the electron-electron pair correlation into a small, symmetric space, yet breaking molecular orbital symmetry by placing the hole initially on a single atom in Hartree-Fock calculation agrees well with the experiment. In principle, by ergodicity, the two descriptions, i.e., (a) the symmetry-restricted dynamic approach with a single time-fluctuating magnetic moment vs (b) the symmetry-broken mean-field approach with spatially fluctuated local moments, are not mutually exclusive but are a choice of representation and, consequently, a choice of computational efficiency, at least if both approaches are carried out exactly. In the exact implementations, (a) dynamic symmetry-restricted and (b) static symmetry-broken ground states should have the same ground state energies [59–63]. In approximate implementations, experience in a two-center molecular system (such as stretched H₂, Li₂, or O₂) indicated that symmetry-broken mean field removes much of what was strong correlation in symmetry-restricted dynamically correlated solutions,


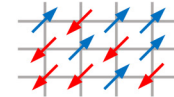
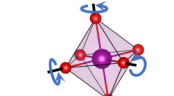
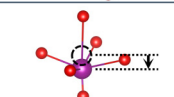
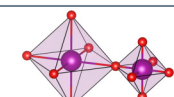
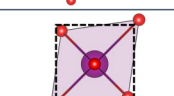
Modality		Symmetry breaking degree of freedom	Schematic	Example in this work
(a) Strong electronic correlation		Electronic symmetry breaking		
(b) Magnetic symmetry breaking		Different local spin configurations		SrVO ₃ (Paramagnetic cubic)
Positional symmetry breaking	(c) Octahedral rotation	Rotation angles		CsPbI ₃ , SrTiO ₃ (Nonmagnetic cubic)
	(d) Atom displacement	Local polarizations		BaTiO ₃ (Antiferroelectric cubic)
	(e) Bond disproportionation	Different octahedral volumes		SrBiO ₃ (Nonmagnetic monoclinic)
	(f) Jahn-Teller distortion	Inequivalent bond lengths		LaMnO ₃ (Antiferromagnetic orthorhombic)

FIG. 1. Modalities of symmetry breaking illustrated for the perovskite structure. From top to bottom: (a) Strong electronic correlation as schematically shown by the Hubbard model (where U is the on-site repulsion and t is the hopping energy); (b) magnetic symmetry breaking such as the paramagnetism (PM), where the lattice sites are occupied by atoms having opposite spins without long-range order; (c) octahedral rotations allowing nonzero rotation angles; (d) atomic displacements such as the ferroelectric displacements in perovskites inducing a local polarization degree of freedom; (e) bond disproportionation allowing octahedra in perovskites to have different volumes; (f) Jahn-Teller distortions elongating the perovskite octahedron along one direction, leading to inequivalent bond lengths between the center and corner atoms.

leaving smaller (“weak”) residual correlation with respect to the exact solution. Thus, a correlation that has been dynamic in the symmetry-restricted case can become static in the symmetry-broken cases, and the correlated methods in symmetry-restricted structures might not be the only way to describe mass enhancement [63]. Symmetry can be restored afterward [64] and often gives localized states but small additional energy lowering. A review of the traditional role of symmetry-broken mean field vis-à-vis symmetry-restricted correlation and that these are nonadditive effects has been recently presented by Perdew *et al.* [63]

Such a symmetry-broken mean-field approach can furthermore provide clear intuition as to the mechanism whereby the electronic structure (here, mass enhancement) is established. The classic picture of the face-centered cubic “empty lattice” band structure having the symmetry of a primitive cell without interactions, as illustrated by Herman [65], shows broad bands and high degeneracies with low masses. Any successive introduction of interaction terms into this empty lattice Hamiltonian (starting with the point-ion pseudopotential) would progressively remove band degeneracies, split broad bands into sets of subbands, and lead to mass enhancement. Examples of known modalities of symmetry breaking that are now shown to lead specifically to mass enhancement are summarized in Fig. 1 and discussed in the following sections. We find that indeed these energy-lowering, mean-field, symmetry-broken modalities (lines 2–6) can enlarge the

band gap and/or contribute to more localized wavefunctions, thus leading to mass enhancements, not only for electrons but also for holes, which were previously attributed exclusively to explicitly correlated methodologies.

The intuition behind this investigation originates from the fact that effective masses can be gleaned qualitatively from $\mathbf{k} \cdot \mathbf{p}$ perturbation theory [66],

$$\frac{1}{m_{n_j}^*} = \frac{1}{m_0} + \frac{2}{m_0^2 k^2} \left(\sum_{l \neq n} \frac{|\langle n\mathbf{0} | \mathbf{k} \cdot \mathbf{p} | l\mathbf{0} \rangle|^2}{E_{n0} - E_{l0}} + \epsilon_{n_j, \mathbf{k}} \right), \quad (1)$$

where $m_{n_j}^*$ is the effective mass of state $|n_j\mathbf{0}\rangle$ at band edge, $\mathbf{0}$ denotes the momentum where the band edge is located, subscript j is the index of degenerated wave functions, m_0 is the free-electron mass, $E_{n0} - E_{l0}$ are interband energy gaps, and $\epsilon_{n_j, \mathbf{k}}$ are the energy shifts from band degeneracy (zero if no degeneracy). The sum is over all eigenstates $|l\mathbf{0}\rangle$. This classic expression shows that the effective mass in solids is generally enhanced by any effects that increase the interband energy gaps ($E_{n0} - E_{l0}$) and/or reduce the wavefunction momentum matrix element $\langle n\mathbf{0} | \mathbf{k} \cdot \mathbf{p} | l\mathbf{0} \rangle$, i.e., producing more compact wavefunctions.

In this paper, we use the textbook definition of the effective mass m^* as the reciprocal of the wave vector curvature $\partial^2 E / \hbar^2 \partial k_i \partial k_j$, except that instead of insisting on an electronic structure based on a symmetry-restricted primitive unit cell, we allow energy-lowering symmetry breaking in a larger

cell. While there is no “theorem,” to our knowledge, showing if DFT can describe exactly band energies, thus effective masses, our justification and indeed method of analysis rely on the insight (but not literal details) from this $\mathbf{k} \cdot \mathbf{p}$ theorem [Eq. (1)], indicating how effective masses are related to band gap. The fact that effective masses are often evaluated from band widths in DFT and in many-body calculations (as implied in previous DMFT [15–24]), as well as in experimental literature [2,3,6,13,14] supports this tradition. Note that the DFT band gap is described as the total-energy difference gap, i.e., the difference between ionization potential $I = E(M-1) - E(M)$ and the electron affinity energy $A = E(M) - E(M+1)$ where M is the number of electrons. Such a total energy difference gap is a proxy to the quasiparticle gap. Since, in this definition, only the ground-state energies are involved, this total energy difference gap can be calculated in principle exactly from DFT and can be directly compared with that measured from experiments [67–69]. Now the quantity that is practically calculated often is the single-particle band gap between conduction band minimum (CBM) and valence band maximum (VBM) $E_{\text{CBM}} - E_{\text{VBM}}$. Reference [69] has shown that such a single-particle gap is equal to the total energy difference band gap for the same XC functional, if the XC is a nonmultiplicative potential (operator is continuous) and the density change is delocalized when an electron or hole is added. This applies to local spin density approximation (LSDA), Perdew-Burke-Ernzerhof (PBE), strongly constrained and appropriately normed (SCAN), and hybrid functionals. The following Secs. III and IV will provide the different definitions of effective mass that have been examined. Our DFT results with symmetry breaking and no dynamic correlation show comparable masses with DMFT and experimental data.

Table I lists mass enhancements calculated by symmetry-broken mean-field DFT in this paper for six compounds compared with experimental observations previously reported for SrVO₃, CsPbI₃, LaMnO₃, and SrTiO₃. Previous DMFT calculations for SrVO₃, LaMnO₃, and SrTiO₃ are also given in Table I. Many of the mass enhancements found by symmetry-broken DFT here are comparable in magnitude with the values suggested by the correlated methods. We see that mass enhancement by symmetry-broken DFT is not unique to open-shell d -electron compounds, and similar magnitudes of mass enhancements also exist for s - p -bonding compounds. This further suggests that viewing the presence of mass enhancement in the considered compounds as evidence for the exclusive need for strong dynamically correlated methodologies [15–24] is not a safe practice before examining the effect of positional and magnetic symmetry breaking on the band structure.

II. APPROACH

A. Supercell model

To allow for inclusion of the pertinent symmetry-lowering effects, the tradition of using the most economical minimal unit cell must be avoided because it might geometrically disallow symmetry breaking. Instead, one should use a

$N_1 \times N_2 \times N_3$ replica of such a minimal cell (i.e., a supercell). Table I shows for each compound (i) the observed low-symmetric ground state at low temperature, (ii) the mass-enhanced phase studied in this paper, (iii) the symmetry-restricted minimal-cell model previously used in the literature. We see that the structure for which mass enhancement was reported in the experiment and studied in previous DMFT calculation is not always the ground-state structure, e.g., for halide perovskites such as CsPbI₃ and oxide perovskite SrTiO₃, the ground states are orthorhombic and tetragonal, respectively, while it is the cubic phase where mass enhancements were reported [4,73]. In such cases where the phase studied is not the ground-state phase, the supercell model is constrained throughout the calculation to have the global lattice symmetry of the phase studied (e.g., cubic), but all internal atomic positions can attain the values that minimize the (constrained) total energy. To assure that the relaxed atomic positions are reliable (e.g., not saddle points on the potential surface), all atoms have been initially “nudged” by applying random atomic displacements (random for both direction and amplitude) before starting the process of following total energy minimization. The size of the supercell is increased until convergence on total energy is found; the cell size is not directly important per se except that certain cells cannot, by symmetry, allow symmetry breaking even if it will lower the energy. This dependence of total energy per atom on the cell size is unique to certain (polymorphous network) compounds but not in conventional materials, such as silicon or ZnSe, where it does not show different total energies between supercell and minimal-cell model. Thus, larger than minimal (super) cells do not necessarily lead to disorder or mass enhancement unless energy lowering takes place.

In all magnetic calculations, the directions of spin moment on every site are collinear and fixed (i.e., spin flip is not allowed), while the amplitudes of magnetic moment are free to evolve during the total energy minimization. In principle, spins can relax during the electron self-consistency calculations to produce nonrandom configurations. We have confirmed that our DFT self-consistent calculations give negligible net magnetization for all AFM and PM structures (<0.001 Bohr magneton per atom).

B. Band unfolding

Whereas the supercell approach has the advantage of allowing the incorporation of local structural and spin motifs, it has the disadvantage of producing a nonintuitive and difficult-to-analyze dense band structure in the small reciprocal-space Brillouin zone (BZ) associated with the large real-space cell dimensions. This difficulty is overcome by applying rigorous band unfolding [74–76] to the supercell band structure, producing effective band structures (EBSs) that replace the sharp bands of ordinary band theory by spectral functions (including both coherent and incoherent components).

C. Calculation of effective mass

We apply four models to calculate the mass and mass enhancement: (1) deducing the mass from the mass tensor

TABLE I. Summary of mass-enhancement factors β_e for electron and β_h for hole compared with experimental observations and DMFT calculations for the compounds investigated in this paper. We provide (i) the observed low-temperature low-symmetry ground states, (ii) the phases studied in this paper for which mass enhancements were reported in the literature, (iii) the symmetry-restricted models used in the literature by DFT and DMFT, (iv) the symmetry-broken modes found presently by DFT in the phases studied, and (v) the mass enhancements found in this paper. Magnetic orders NM, AFM, and PM denote nonmagnetic, antiferromagnetic, and paramagnetic, respectively. Here, several different DMFT values are given for comparison because the DMFT calculated mass enhancement depends on the U value and the method to remove the double-counting potential. For cubic CsPbI₃, to the best of our knowledge, there are no experimental reports for separate electron and hole masses, and only reduced mass $m_r^* = -m_e^*m_h^*/(m_e^* + m_h^*)$ has been reported for CsPbBrI₂ [70]; our result is therefore compared with such experimental reduced mass.

Compound	Ground state	Phase studied in this paper	Symmetry-restricted model (ref. $\beta = 1$)	Symmetry-broken mode found by DFT	Mass enhancement	
SrVO ₃	PM cubic	PM cubic	NM $Pm\bar{3}m$	Magnetic symmetry breaking	β_e	DFT: 1.5 ± 0.1 (exp.: $1.3^a, 2.2^b, 2.9^b$, DMFT: 1.8 ± 0.2^c)
					β_h	DFT: 1 (exp.: 1^d)
CsPbI ₃	NM orthorhombic	NM cubic	NM $Pm\bar{3}m$	Octahedral rotation	β_e	DFT: 1.8^e , (exp.: $m^* = 0.12m_0^e$)
					β_h	DFT: 2.2^e , (exp.: $m^* = 0.12m_0^e$)
LaMnO ₃	AFM orthorhombic	AFM orthorhombic	AFM $Pnma$ (no Jahn-Teller)	Jahn-Teller distortion	β_e	DFT: 1.8 ± 0.5
					β_h	DFT: 1.6 ± 0.4 , (exp.: $2.6-2.8^f$, DMFT: $1.3-1.7^g$)
SrBiO ₃	NM monoclinic	NM monoclinic	NM $P2_1/n$ (no disproportionation)	Bond disproportionation	β_e	DFT: 1.3 ± 0.2
					β_h	DFT: 1.5 ± 0.2
SrTiO ₃	NM tetragonal	NM cubic	NM $Pm\bar{3}m$	Octahedral rotation	β_e	DFT: 1.1, (exp.: $2-3^h$, DMFT: 1^h)
					β_h	DFT: 1.1
BaTiO ₃	NM rhombohedral	NM cubic	NM $Pm\bar{3}m$	Ferroelectric displacement	β_e	DFT: 1.1
					β_h	DFT: 1

^aReference [16].

^bReference [17].

^cReferences [11,12,14].

^dEstimated from Ref. [71].

^eDFT calculated reduced mass $m^* = 0.14m_0$, and experimentally measured reduced mass (for cubic CsPbBrI₂) $m^* = 0.12m_0$ [70].

^fReference [72].

^gBy comparing this paper with Ref. [53].

^hReference [73].

of the reciprocal for the second derivative of E vs \mathbf{k} at the band edges; if the mass tensor is anisotropic ($m_1^* \neq m_2^* \neq m_3^*$), the result mass will be calculated as $m^* = (\frac{1}{m_1^*} + \frac{1}{m_2^*} + \frac{1}{m_3^*})^{-1}$; (2) deducing the mass from the DOS at Fermi level $m^* \propto [D(E_F)]^{2/3}$; (3) deducing the mass from the slope of bands at Fermi level, i.e., the Fermi velocity (v_F), as $m^* \propto \frac{1}{v_F}$; and (4) deducing the mass from the bandwidth $m^* \propto \frac{1}{W}$. Note that method (1) can give the absolute mass, while methods (2)–(4) are used only for the relative mass-enhancement factor $\beta = m_{\text{Theory}}^*/m_{\text{model}}^*$ but not the absolute mass. We focus here on the mass-enhancement factors (relative masses) rather than on the absolute values of masses.

III. MAGNETIC POLYMORPHOUS NETWORK IN PARAMAGNETS LEADS TO MASS ENHANCEMENT: SrVO₃

A. Representation of the PM phase as a distribution of local spin environment

All calculations reported here are spin-polarized, allowing up and down spins. In addition, we allow for spatial spin symmetry breaking: the PM phases of $3d$ oxides are often described in the DFT literature as being NM, interpreting the PM condition of globally zero moment on an atom-by-atom basis, deducing that each atom must be NM [12–18,53–55]. This strong restriction does not follow from the definition of

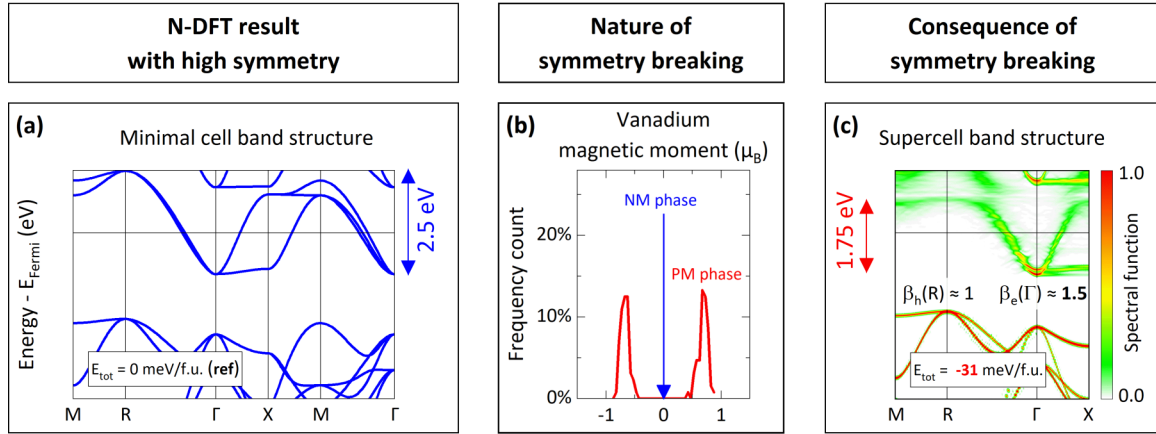
SrVO₃ (paramagnetic cubic phase, PBE+U)

FIG. 2. Mass enhancements in the paramagnetic (PM) cubic phase of SrVO₃. (a) The band structure obtained from the same naïve density functional theory (N-DFT) restriction as in previous literature [12–18], namely a single-cell, cubic, nonmagnetic (NM) SrVO₃ model using PBE + U ($U = 1.25$ eV on V d orbitals). (b) The distribution of spin moments in the present PM phase: blue lines show that, in the minimal-cell NM phase, all vanadium sites have zero magnetic moment, while the red curve shows that, in the PM phase, different vanadium sites have a distribution of different, nonzero magnetization. (c) The unfolded band structure when removing the minimal-cell restrictions by using instead a cubic, 128 f.u. PM supercell SrVO₃ with the same PBE + U method. The total internal energy E_{tot} from DFT of (c) is 31 meV per formula unit (meV/f.u.) lower than that of (a). Masses in (c) are calculated via density of states (DOS) at Fermi level (which gives $\beta_e = 1.4$ – 1.6 and $\beta_h = 1$; the subscripts e and h denote the electron and hole mass enhancements; uncertainty is due to the variation of DOS nearby the Fermi level), second derivative of E vs \mathbf{k} (which gives $\beta_e = 1.46$ and $\beta_h = 1$), and bandwidth (which gives $\beta_e = 1.43$ and $\beta_h = 1$). The vertical arrows in (a) and (c) show the bandwidths. The same PBE + U method has been applied for all SrVO₃ calculations.

PM or from the DFT, and as was recently recognized, it leads to rather high total energy [27]. A correct description of PM entails allowing a larger (super) cell that can accommodate different local spin environments should they lower the total (DFT) energy. For example, in a PM crystal where each magnetic ion is locally coordinated by N other magnetic ions, one can have in the collinear description a distribution of local spin environments, e.g., an up-spin ion can be coordinated by $(N-m)$ up-spin ions plus m down-spin ions, where $0 \leq m \leq N$; if the up and down orientations are chosen randomly (which corresponds to the high-temperature limit of the PM phase), it follows the binomial statistics, i.e., finding an ion with m down-spin neighbors follows the probability distribution function $P(m; N, 0.5) = \binom{N}{m} 0.5^N$. This model of PM local order represents a generalization of the AFM spin configuration that includes a single local environment (e.g., up-spin site coordinated only by down-spin sites), whereas in the PM phase, the above-noted additional local environments could exist. This is accomplished in practice by borrowing an idea known from the theory of substitutional $A_x B_{1-x}$ alloys [77]: construct an M -atom supercell for composition x with sites occupied by A - and B -type atoms (here, up-spin and down-spin atoms), so that the atom-atom correlation function will mimic for a finite supercell a given statistic for the infinite cell (here, random binomial statistics) the best possible way for an M -atom supercell. Such special quasirandom structures (SQSs) identify the most economical supercells for given size M . We currently use the random spin-spin correlation (corresponding to the high-temperature limit), although the use of nonrandom short-range order (SRO) in SQS is possible [78,79].

We consider next the PM phase of SrVO₃ modeled by a 128 f.u. supercell (i.e., 640 atoms per cell) with collinear up- and down-spin configuration. Figure 2(b) shows in red the

distribution of DFT calculated up-spin and down-spin magnetic moments, whereas the single vertical blue line shows the all-site-having-zero-spin condition in the minimal-cell NM case. For all relaxed SrVO₃ supercells, we have found negligible atomic displacement, consistent with the fact that the size mismatch factor revealed by the Goldschmidt factor is negligible. Comparing different spin configurations including ferromagnetic (FM), AFM, and PM phases in SrVO₃ (Table II in Appendix B) shows nearly degenerate total energy, suggesting that the spin ground state could be a mixture of many possible magnetic orders, i.e., in agreement with experiment [80,81] that SrVO₃ is a PM metal down to low temperatures and does not form magnetic order. Note that all magnetic phases show significant energy lowering when compared with the conventional NM model.

B. Electron mass enhancement in SrVO₃

Figure 2(a) shows the N-DFT band structure (cubic unit cell containing a single f.u., no relaxation, with NM spin configuration having zero moments at all sites) giving a metallic phase, with a conduction bandwidth of 2.5 eV. This model was used for m_{model}^* in many previous studies [12–17] to calculate mass enhancement using, e.g., DMFT and GW theories. Figure 2(c) shows the spectral functions calculated in DFT from such a 640 atom supercell unfolded into the primitive BZ of SrVO₃. The unfolding procedure used in Fig. 2(c) allows one to reduce the band structure complexity of a supercell, converting the sharp bands from the monomorphous case to an EBS having a finite band spread that depends on the distribution function used to describe the spin in a PM supercell (in the current case, we neglect the spin-spin SRO, so the fuzziness may be overestimated). Figure 3 shows the

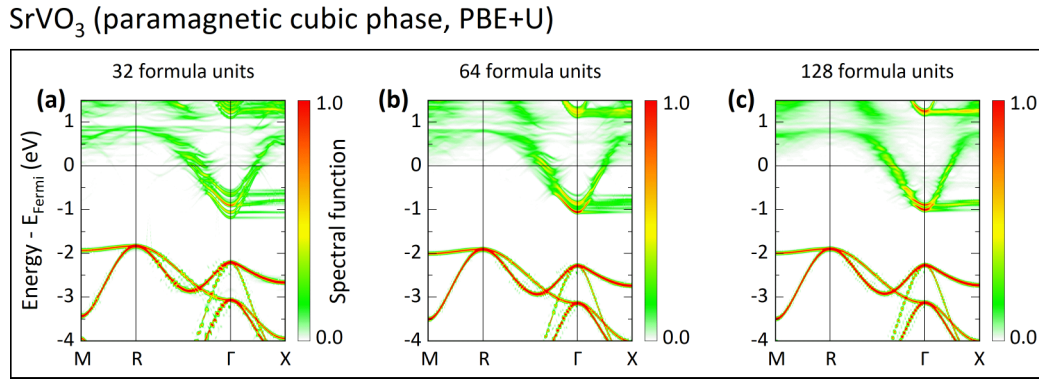


FIG. 3. Convergence of mass enhancement and band structure of SrVO₃ paramagnet (PM) vs supercell size increasing from 32 f.u. (160 atoms), to 64 f.u. (320 atoms), to 128 f.u. (640 atoms). All supercells are generated by using the spin special quasirandom structure (SQS) method. Note band narrowing convergence.

evolution of the unfolded band structure as the real-space supercell size increases, finding convergence.

The significant result is that the conduction band in the PM phase, allowed to have a distribution of local spin motifs, is narrowed relative to the minimal-cell NM case from 2.5 eV [Fig. 2(a)] to 1.75 eV [Fig. 2(c)]. This leads to an electron mass-enhancement factor (β_e) in the PM supercell $\beta_e(\text{DFT/N-DFT}) = 1.43$. Note that different definitions of effective mass give somewhat different results: the bandwidth mass enhancement of 1.43 can be compared with the DOS mass enhancement 1.4–1.6 at Fermi level, while the second derivative of E vs \mathbf{k} at the conduction band edge gives 1.46. Note that we have not attempted to fit the result by adjusting U , although the choice of more localizing XC functional can increase the enhancement factor. We note that, whereas the values obtained depend somewhat on the definition of effective mass used, the lattice constant (here, we used $a = 3.83 \text{ \AA}$), and the U value, allowing for polymorphous spin configuration, leads in all cases to an enhancement factor of 1.5 ± 0.1 . These calculated mass enhancements are comparable with the experimentally measured factor $\beta_e(\text{exptl/N-DFT}) \approx 1.8 \pm 0.2$ [11,12,14], while smaller than the enhancement factors from DMFT, e.g., $\beta_e(\text{DMFT/N-DFT}) = 2.9$ [17] (using a much larger $U = 5.5 \text{ eV}$ that narrows bands further) and from GW + DMFT $\beta_e = 1.3$ [16], 2.2 [17] (where the two values correspond to different versions of accounting approximately for the double-counting error in GW + DMFT).

C. Hole mass enhancement in SrVO₃

The DFT calculations naturally provide all bands with equal approximations, both the electron conduction band (mainly V d orbitals) and the valence hole band (mainly O p orbitals). We find no mass enhancement for hole states in the principal valence band, consistent with the fact that the spin configuration in the O p -like principal valence band corresponds to a closed electronic shell and negligible magnetic moment that show no distribution of motifs. We will see later that, in ABX_3 perovskites, where the local environment is made of a distribution of positional motifs rather than from spin motifs, there will be both electron and hole mass enhancements.

D. Analysis of the contributing factors to spin-induced mass enhancement in SrVO₃

The real-space symmetry-broken supercell approach provides for an intuitive understanding of the results. The degree of freedom within our PM supercell is the local spin configuration (as we have found that the positional relaxation is negligible in this system). A local spin motif consists at the first order of a central $3d$ atom and its first-shell $3d$ (next nearest) neighbors. Whereas in the case of the minimal-cell NM model, each and every motif has zero spin, and in the case of AFM order, each motif has maximum dissimilarity between the spin of the central atom and the spins of its coordination shell (e.g., the AFM-G-like local motif when the central atom is up-spin, while all its neighbors are all down-spin), in our model of the PM phase, each spin can have a local distribution of spins, including the case of maximum similarity (e.g., the FM-like local spin motif when the central atom is up-spin, and so are all its neighbors), maximum dissimilarity, or any configurations in between. Figures 4(a)–4(c) show the random (high-temperature limit) statistical weight for each spin motif. Each local spin motif might have its unique, projected local DOS. The vertical arrows in Figs. 4(d)–4(i) indicate that each local spin motif contributes differently to the conduction bandwidth, whereas the reference minimal-cell result using the NM model [shown in Fig. 4(d)] has considerably wider DOS. Figures 4(e)–4(i) show that the locally AFM-G-like vanadium sites with maximum spin dissimilarity with their neighbors have the most compressed DOS [Fig. 4(i); smallest range in energy and the highest peak in DOS, indicating enhanced electron mass], while the locally FM-like sites with maximum spin similarity with the neighbors have the most expanded DOS [Fig. 4(e); similar to the bandwidth in the NM model in Fig. 4(d), hence not contributing to mass enhancement]. Figure 4 suggests that the mass enhancement depends on spin SRO, i.e., the spin configuration at the center site and the neighbors, through the statistical weight for each spin motif [Fig. 4(b)]: an AFM-like, anticlustering SRO can lead to a larger enhancement coefficient β , while a FM-like, clustering SRO can reduce β . This analysis shows that the existence of a polymorphous distribution of spin-polarization motifs with their attendant, different local DOS contributing differently

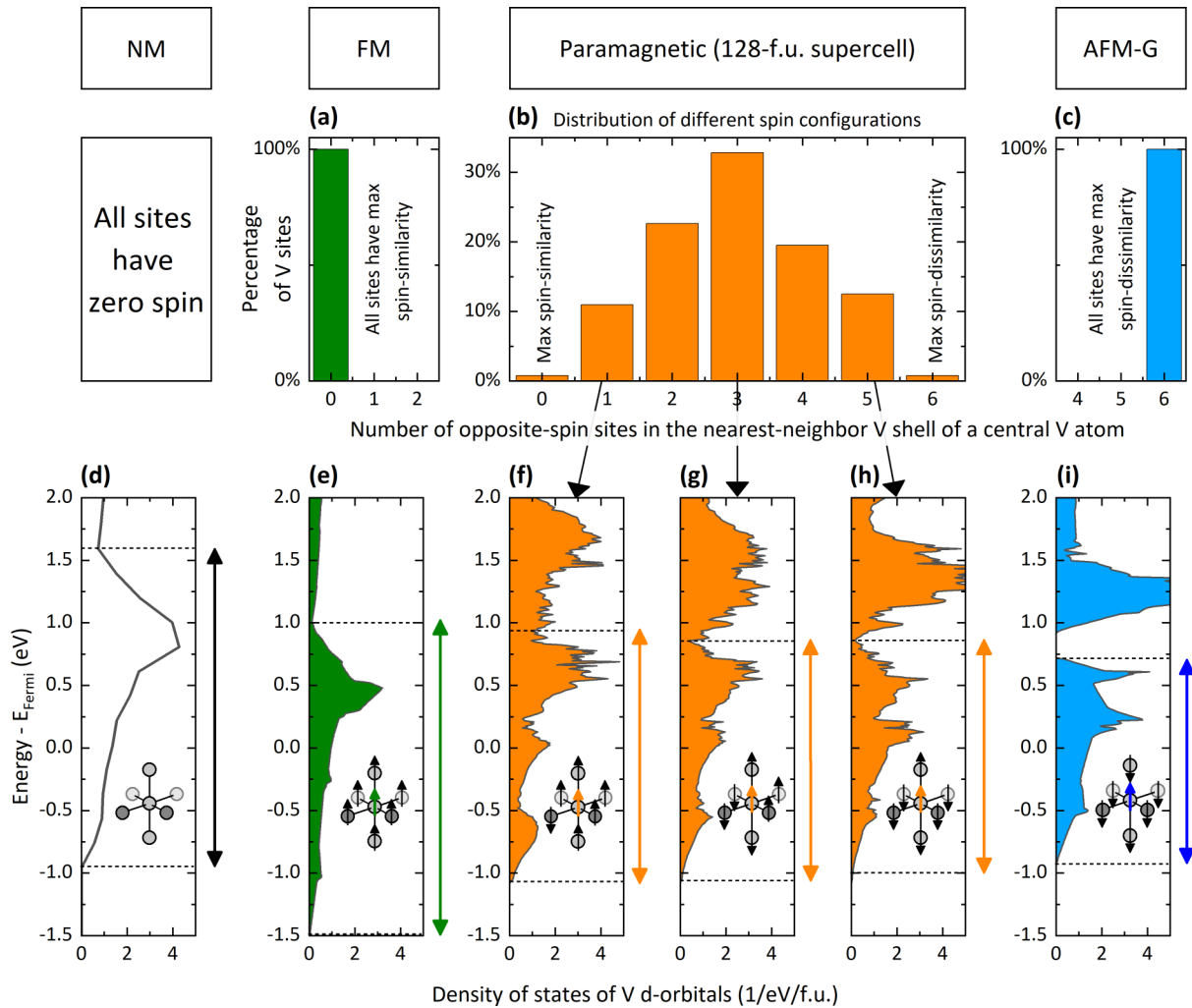


FIG. 4. Total density of states (DOS) of cubic SrVO_3 (the same PBE + U method) as a weighted superposition of the partial DOS (PDOS) of the local spin motifs. Upper panel: the weight of local spin configuration in: (a) statistical weights of ferromagnetic (FM) primitive cell [all the first-neighbor vanadium have the same spin direction as the center vanadium, see insert in (a)]; (b) distribution of statistical weights of different spin configurations in the cubic paramagnetic (PM) supercell; (c) statistical weights of G-type antiferromagnetic (AFM-G) double perovskite cell [all the first neighbor vanadium have the opposite spin direction to the center vanadium, see insert in (c)]. Lower panel: the vanadium *d*-PDOS in different spin configurations: (d) nonmagnetic (NM) primitive cell in which each site has zero spin; (e) FM motif; (f)–(h) different local spin motifs in PM phase, and (i) AFM-G motif. The dash lines and vertical arrows in (d)–(i) show the bandwidths of the *d* orbital for guide of eyes. Note that, in (d)–(i), we only show the *d*-PDOS of the central vanadium atoms (neighbors are not included to avoid multiple counting).

to the total DOS creates the possibility of spin-induced mass enhancement.

As discussed above, static DFT calculations permitting symmetry breaking and ensuing creation of local spin motifs naturally show mass enhancement. The scope of the current calculation of E vs \mathbf{k} dispersion does not extend, however, to fully model angle-resolved photoemission spectroscopy (ARPES) spectra, including ARPES matrix element effects [82,83], or lifetime effects [84,85] associated with the observed sharpening of the ARPES states as they approach the Fermi level [12–14]. Description of lifetime broadening generally requires a time-dependent dynamics analysis, e.g., spin dynamics combined with molecular dynamics, possible in the mean-field DFT framework [86].

IV. POSITIONAL SYMMETRY BREAKING CAUSES COUPLING OF THE ELECTRONIC BANDS LEADING TO MASS ENHANCEMENT

A. Octahedral rotation enhances masses in *s-p* halide perovskite CsPbI_3

Octahedral tilting (rotations) [43] have been known to exist in perovskites; here, we point out that such observed local modes can cause mass enhancement. The perovskite structure consists of corner-sharing octahedra that allow octahedral rotation and tilting. The classic atomic size mismatch between the *A* and *B* sublattices in ABX_3 drives static octahedral tilting and rotations, as was recognized in Ref. [87] and verified by modern PDF measurements [88] as well as by DFT total energy minimization [52,89–92]. This kind of deformation

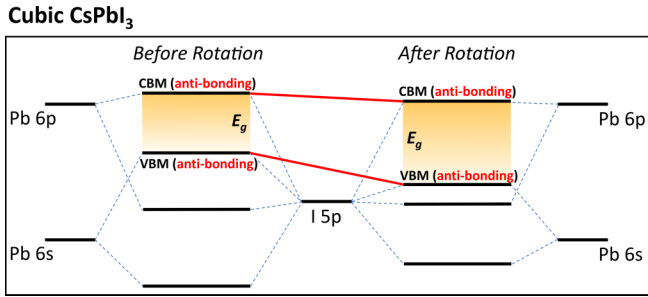


FIG. 5. Energy level diagram for CsPbI₃, before and after octahedral rotation. The red solid lines show the trends of band gap change.

derives from classical atomic size mismatch and therefore exists even in close-shell *s-p* electron compounds such as halide perovskites [52,90,91]. Octahedral tilting (rotation) effects have been investigated in lead and tin halide perovskites for the low-temperature tetragonal and orthorhombic phases. However, for the cubic phase, it has been generally assumed [30–33] that, because of its XRD designation as a $Pm\bar{3}m$ structure with a single f.u. per cell, such tilting is disallowed by symmetry, hence absent. Here, we point out that (i) a minimal $2 \times 2 \times 2$ cubic supercell is needed to reveal tilting, (ii) single tilting modes [43] already change the mass, and (iii) larger supercells such as $4 \times 4 \times 4$ can reveal multimode tilting, showing further lowering of the total energy relative to the monomorphous $Pm\bar{3}m$ cubic model. Such multimodes significantly affect mass enhancement. Although, technically, this can be posed as an electron-phonon effect, given that the pattern of tilting and atomic displacements are complex and imply the participation of a significant number of phonons, we do not use the phonon terminology; instead, we explicitly (and nonperturbatively) minimize the generally anharmonic DFT energy surface with respect to all atomic positions, dislodge atoms from metastable local positions to stable positions, then calculate the ensuing band structure and masses.

1. Qualitative analysis of how octahedral tilting affects band edge energies in CsPbI₃

The coupling between octahedral tilting and electronic structure in low-temperature phases has been discussed in oxide [5] and halide perovskites [30] as a band-gap-tuning mechanism. Here, as schematically shown in Fig. 5, we demonstrate how the octahedral rotation in the *s-p* bonded compound CsPbI₃ affects band edge states. In cubic CsPbI₃ without distortion, the valence band maximum (VBM) is an antibonding state formed from the Pb *s* and I *p* orbitals, while the conduction band minimum (CBM) is weakly antibonding state of Pb *p* and I *p* orbitals. Allowing rotations of the (PbI₆) octahedron weakens both the *p-p* and *s-p* bonding between Pb and I. Consequently, being antibonding states, both CBM and VBM move to lower energies. However, because the VBM is more sensitive to octahedral deformation (being composed of inner-shell 6*s*-3*p* antibonding) than the CBM (being composed of outer-shell 6*p*-3*p* antibonding) [93], the VBM moves further than CBM, leading to a larger band gap due to rotation (Fig. 5, right panel).

2. Model DFT calculations on the effect of frozen rotations on mass enhancement in CsPbI₃

The results of the simple model of Fig. 5 are then validated by DFT calculations of small (8 f.u.) model supercells, where we artificially impose given octahedral rotation angles, followed by band unfolding to the single-cell cubic primitive BZ. The unfolded band structure is shown in Fig. 6. The imposed octahedral rotation here is $a^+a^-a^-$ mode (Glazer notation [43]) or $M_2^+ \oplus R_5^-$ (irreducible representation from Miller and Love [94]). The imposed octahedral rotations can affect the curvature of both valence and conduction bands at the band edges. Choosing the band gap and effective masses of the zero-rotated structures as the reference, as shown in Fig. 6, one can see that, under a uniformed arbitrary rotation of (10°, 10°, 10°), the band gap of CsPbI₃ increases by 0.52 eV (~40%), and the electron and hole masses are enhanced by 77% and 113%, respectively.

3. Full supercell calculation of rotation-induced mass enhancement in CsPbI₃

Having clarified the effect of classical rotation on the band structure by the model (Fig. 5) and validated it by DFT (Fig. 6), we next study a large supercell with optimized rotating geometries in the cubic phase of CsPbI₃. Recall that the rotations discussed here are not thermal, but in fact, they are energy-lowering distortions derived by the nature of the chemical bonds (here, steric effects) even at low temperatures. Thus, we obtain these deformations by minimization of the DFT internal energy. However, this requires that we allow a larger-than-the-minimal unit cell so that rotations can be accommodated geometrically. The electronic structure of a single-cell cubic ($Pm\bar{3}m$) model (monomorphous model) is shown in Fig. 7(a). Restricted by the small size and periodic boundary condition, such a structure cannot accommodate rotations [as shown by the blue lines in Fig. 7(b)]. We avoid such a restrictive assumption using a supercell representation (32 f.u. supercell) instead. We perform a constrained minimization of the internal energy ($T = 0$) of the cubic phase that retains the macroscopic cubic supercell shape (or else the minimization will converge to the ground-state orthorhombic or tetragonal structures that are not the subject of the current study). At the same time, we allow all cell-internal degrees of freedom to locally adjust to find the structure with the lowest total energy. This is done by using a set of random initial nudging to dislocate atoms from possible local minima.

It has been shown in our recent paper [36] that, for lead halide perovskites with organic molecules on the *A* site, such a supercell representation following the constrained DFT total energy minimization explains various anomalies in the cubic phase, where the minimal-cell model disagrees with experimental observation. This includes a close agreement with the measured PDF, significant increase in the band gap, and dielectric constant. For the cubic CsPbI₃ supercell, we have found that, when abandoning the restriction of the minimal-cell model, the atomic configuration of cubic phase that gives the lowest total energy of the cubic phase (the supercell outshape has been constrained to be cubic) is not the single f.u. $Pm\bar{3}m$ cubic model but a supercell representation for the cubic phase with many local octahedral tilting. The many

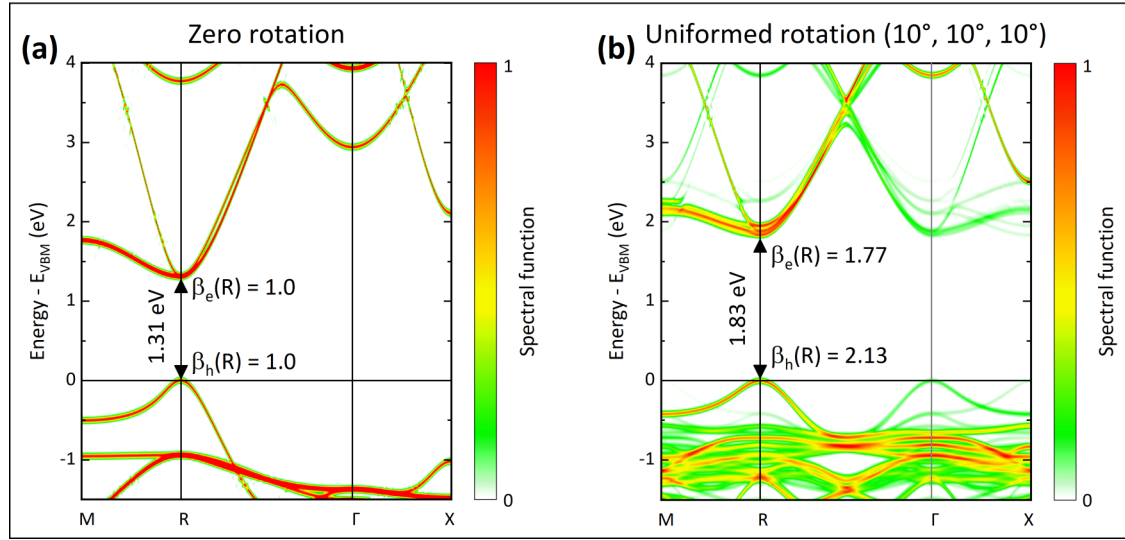
CsPbI₃ (nonmagnetic cubic phase + artificial tilting, PBE)

FIG. 6. The unfolded spectral function [effective band structure (EBS)] in the cubic primitive Brillouin zone, (a) before and (b) after a uniformed ($10^\circ, 10^\circ, 10^\circ$) $a^+a^-a^-$ rotation for cubic CsPbI₃. Both (a) and (b) are calculated using the 8 f.u. supercell. Note that EBS shown in (a) is identical to the band structure obtained from a minimal-cell cubic model because (a) has no atomic distortion. Band gap is 1.31 eV in (a) and 1.83 eV in (b). Taking effective masses of CBM and VBM in (a) as references, the mass-enhancement factors in (b) are $\beta_e = 1.77$ (for electron, counting all three states near CBM) and $\beta_h = 2.13$ (for hole), respectively. All masses come from band dispersion (second derivative of E vs \mathbf{k}).

local tilts in the cubic supercell cannot be written using the simple Glazer notations but must involve complex notations [43] and cannot be reduced into smaller cell models. We find that (i) the rotation angles are distributed among $5\text{--}13^\circ$ [red lines in Figs. 7(b) and 7(e)]; (ii) the supercells have lower total energy (-124.4 meV/f.u.) compared with the single-cell model. Recall that, during the DFT calculation, we used

the equivalent k-point mesh for all cells ($12 \times 12 \times 12$ Γ -center k-point mesh in primitive cubic BZ) and a total energy tolerance of 10^{-8} eV/atom. We therefore suggest that the -124.4 meV/f.u. energy lowering is robust. Furthermore, (iii) we find, as expected from the simple model of Fig. 5, a significant band gap increase and thus mass-enhancement factors: the band gap increases from 1.31 eV in the monomor-

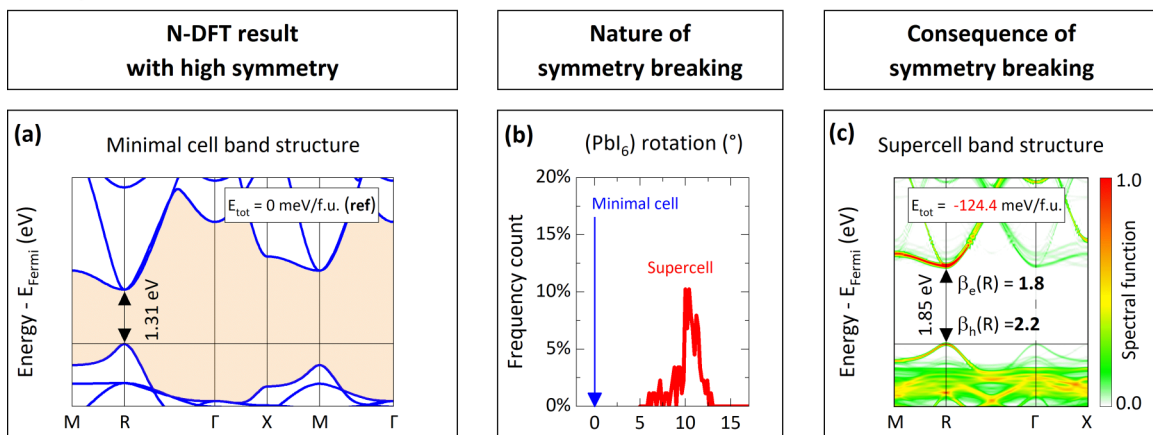
CsPbI₃ (nonmagnetic cubic phase, PBE)

FIG. 7. Mass enhancements in cubic CsPbI₃. (a) The band structure from the same naïve density functional theory (N-DFT) restriction as in previous literature [30–33], namely a single-cell cubic model, using PBE functional. (b) The distribution of octahedral rotation angles. The blue arrow in (b) shows that, in the minimal-cell model, all octahedra have zero rotation, while the red curve shows that, in the supercell, different octahedra have a distribution of different, nonzero rotations. (c) The unfolded band structure when removing the minimal-cell restrictions by using instead a cubic, 32 f.u. supercell CsPbI₃ with the same PBE method. Masses in (c) are calculated via the second derivative of E vs \mathbf{k} , which gives $\beta_e = 1.8$ and $\beta_h = 2.2$. To the best of our knowledge, the experimental measurement for separate electron and hole masses for cubic CsPbI₃ has not been reported yet; while for cubic CsPbBrI₂, the reduced mass $m^* = -m_e^*m_h^*/(m_e^* + m_h^*)$ has been reported as $0.12m_0$, very similar to the reduced mass calculated from (c), which is $0.14m_0$, but 1.8 times heavier than the reduced mass from (a), which is $0.07m_0$.

phous single-cell model to 1.85 eV in the polymorphous supercell model (the measured band gap is $E_g = 1.73$ eV [30]) leading to mass enhancements $\beta_e = 1.8$ and $\beta_h = 2.2$ for electrons and holes, respectively [Figs. 7(a) and 7(c)]. Although, as far as we know, the effective mass has not been reported from experiments for cubic CsPbI₃, the reduced mass [$m^* = -m_e^* m_h^* / (m_e^* + m_h^*)$] for cubic CsPbBrI₂ has been measured [70] as $m^* = 0.12 \pm 0.01 m_0$, which is close to our prediction (masses are calculated via the second derivative of E vs \mathbf{k}), here, $m^* = 0.14 m_0$ using symmetry-broken DFT. Recall that neglecting the distortions gives a mass 1.8 times smaller. We conclude that semiclassical octahedral rotations in ABX_3 can derive quantum mechanical band gap increases and significant mass enhancements. The same physics is expected to contribute to oxides; the magnitude of the effect would naturally depend on the extent of rotations and the response of the host crystal to deformations.

B. Jahn-Teller-like Q_2^+ distortion enhances masses in LaMnO₃

To draw the analogy between mass enhancement in *s-p* bonding perovskites (previous section) and the better-known effect in *d*-electron perovskites, we treat next the compound LaMnO₃. The observed positional symmetry breaking in orthorhombic LaMnO₃ is a pseudo-Jahn-Teller distortion, leading to inequivalent Mn-O bond lengths in the MnO₆ octahedron. It has been previously argued that such a Jahn-Teller distortion is specifically attributed to dynamic correlations [53] and that mean-field DFT fails to predict the ensuing structural or electronic properties [95]. Previous DFT + U calculations reproducing the Jahn-Teller distortion in the orthorhombic LaMnO₃ [96–98] gave perhaps the impression that the presence of + U in DFT implies the same correlation role as + U in the Hubbard Hamiltonian. More recently, Varignon *et al.* [99] showed that DFT without U is already enough to capture such distortions, provided that a more accurate XC functional was used. It was also clarified [100] that proper Jahn-Teller distortion is associated with degeneracy removal (i.e., electronic instability such as the Q_2^- mode [101]), whereas the Q_2^+ mode [101] originates from classic steric effects (the Goldschmidt tolerance) that can be classified as pseudo-Jahn-Teller distortions. Here, we show that such modes cause mass enhancement.

Figures 8(c) and 8(d) show the atomic structure and band structure of an orthorhombic AFM cell with Q_2^+ deformation taken from previous DFT calculation [100]; while Figs. 8(a) and 8(b) show the atomic structure and band structure of the same AFM cell (the same AFM order, the same octahedral rotation and octahedral volume) as (c) and (d) but only removing the Q_2^+ deformation. Such a Q_2^+ -free model [Figs. 8(a) and 8(b)] has been used as the DFT model in previous studies, giving metallic behavior [53,102,103]. In this work, for all LaMnO₃ calculations we used the SCAN functional. The band structure lacking the Q_2^+ mode (b) is metallic, while the band structure with Q_2^+ mode (d) is gapped. Using (b) as the reference and considering the bandwidths of Mn *d* e_g bands in (d), the bandwidth enhancement factors is $\beta_e = 1.8 \pm 0.5$ and $\beta_h = 1.6 \pm 0.4$ for electrons and holes, respectively; the uncertainty is because bandwidths along different \mathbf{k} paths give different enhancement factors. The enhancement factor

LaMnO₃ (orthorhombic AFM phase, SCAN)

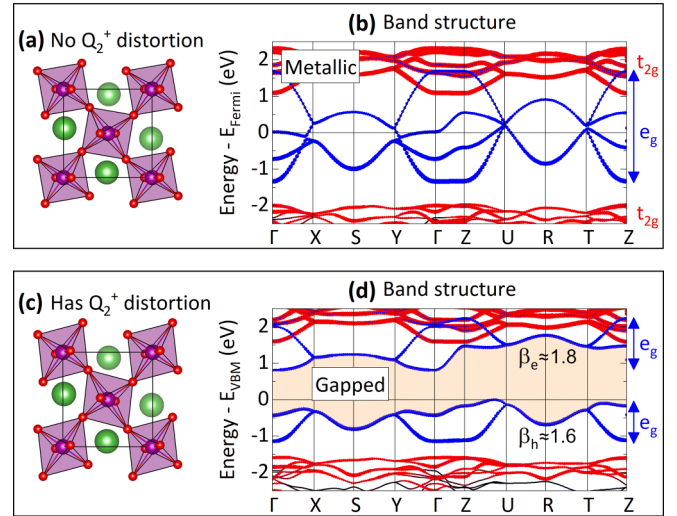


FIG. 8. Mass enhancements in antiferromagnetic (AFM) orthorhombic phase of LaMnO₃. (a) The atomic structure and (b) the band structure with no Jahn-Teller-like Q_2^+ distortion, using the SCAN functional. The system is metallic and has a broad Mn e_g band [bandwidth is denoted by the blue arrow on the right side of (b)] crossing the Fermi level. (c) The atomic structure and (d) the band structure when considering the correct Q_2^+ distortion with the same SCAN functional, where the gap opens between the two Mn e_g bands [bandwidths are denoted by blue arrows on the right side of (d)]. Red and blue circle symbols in (b) and (d) denote the orbital projections of Mn *d* t_{2g} and e_g orbitals, respectively; other orbitals are not shown here; the size of the circle is proportional to the composition of orbital. Mass enhancements in (d) with respect to (b) are calculated via the bandwidths of Mn e_g bands, which give $\beta_e = 1.8 \pm 0.5$ and $\beta_h = 1.6 \pm 0.4$ (uncertainty is because bandwidths along different \mathbf{k} paths give different enhancement factors).

obtained by DMFT with Q_2^+ deformation is $\beta_h = 1.3$ – 1.7 (values are extracted by comparing this work with results reported in DMFT Ref. [53]) and comparable with experimental observation of $\beta_h = 2.6$ – 2.8 in La_{0.6}Sr_{0.4}MnO₃ [72]. We conclude that the pseudo-Jahn-Teller distortion Q_2^+ captured by mean-field DFT is capable of producing significant mass renormalizations, even though in this case both DFT and DMFT give smaller renormalization than what was measured, which may be due to the A-site alloy effect in the measured sample La_{0.6}Sr_{0.4}MnO₃ [72].

C. Bond disproportionation enhances masses in SrBiO₃

Bond disproportionation in perovskites corresponds to the spontaneous transformation of two equal octahedra into two inequivalent octahedra, also known as octahedral breathing distortion, belonging to M_1^+ or R_1^+ mode [104]. A cell model of ABX_3 containing a single f.u. allows obviously a single volume for all (BX_6) octahedra, while some compounds, e.g., SrBiO₃ and BaBiO₃ [29] prefer bond disproportionation on B ions, appearing as some octahedra dilate while others contract, eventually leading to multiple local environments instead of a single local environment. Total energy calculations [105] show that this disproportionation is energy lowering.

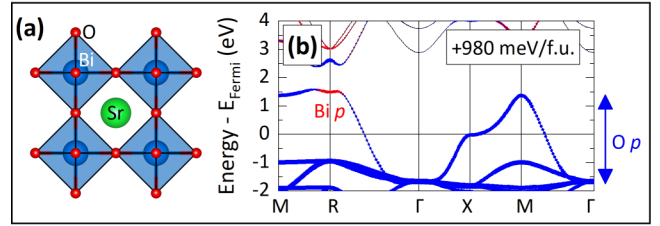
We choose SrBiO₃ as an example to investigate such a bond disproportionation effect on effective masses. SrBiO₃ is known to be insulating in its low-temperature monoclinic phase with a disproportionate R_1^+ distortion [106]. The monoclinic phase shows a tilting $M_3^+ \oplus R_4^+$ mode (Glazer notation $a^+b^-c^-$), which could also contribute to the mass enhancement. To isolate the contribution of R_1^+ disproportionation from tilting, we apply here a three-level model: (1) we start from a level 1 model, which is minimal-cell cubic $Pm\bar{3}m$ structure; (2) then we apply a tilting $M_3^+ \oplus R_4^+$ mode to construct a level 2 monoclinic ($P2_1/n$) structure without disproportionation; and (3) finally, a level 3 model uses the experimentally observed SrBiO₃ monoclinic phase (also $P2_1/n$) with both tilting (the same amplitude as in level 2) and disproportionation. The atomic structures, together with the band structures using the PBE functional + spin-orbit coupling (SOC) effect for these three levels, are shown in Fig. 9.

(1) Level 1 [$Pm\bar{3}m$ cubic; Figs. 9(a) and 9(b)] is a p-type degenerate metal, as its Fermi level crosses its wide [as denoted by the blue arrow on the right side of Fig. 9(b)] principal valence band made of O p orbitals. The total DFT energy of level 1 is extremely high (+980 meV/f.u. above the convex hull), clarifying that it is not a low-temperature ground state. (2) Level 2 monoclinic phase without disproportionating R_1^+ distortion [Figs. 9(c) and 9(d)] shows a more compact O p valence band; however, it is still a p-type gapped metal, i.e., the octahedral tilting cannot open the gap. The total DFT energy of level 2 is 71 meV/f.u. above the convex hull. (3) Finally, level 3, the monoclinic phase with disproportionate R_1^+ distortion [experimental structure; Figs. 9(e) and 9(f)], shows semiconducting behavior with a 0.26 eV gap between the two split O p bands, a splitting induced by the bond disproportionation. Level 3 is at on the convex hull (i.e., the ground state). Nevertheless, as seen in Fig. 9, the disproportionating R_1^+ distortion is the key to band gap opening; therefore, the most interesting mass enhancement is the one from level 2 to level 3 $\beta(L3 : L2)$. Considering the bandwidths of O p bands in Figs. 9(d) and 9(f), if using Fig. 9(d) as the reference, the bandwidth-related masses in Fig. 9(f) have the enhancement factors of $\beta_e(L3 : L2) = 1.3 \pm 0.2$ and $\beta_h(L3 : L2) = 1.5 \pm 0.2$; the uncertainty is because bandwidths along different \mathbf{k} paths give different enhancement factors. We conclude that disproportionation symmetry breaking, an effect that exists both in s - p perovskites as well as in d -electron perovskites, is capable of significant mass enhancement.

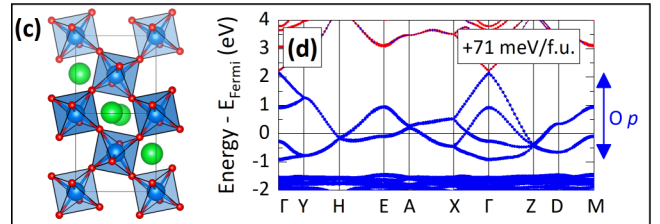
V. NOT ALL POSITIONAL SYMMETRY BREAKINGS LEADS TO SIGNIFICANT MASS ENHANCEMENT

The examples shown in Secs. IV A, B, and C indicate cases where symmetry breakings result in large energy-lowering, and they couple significantly to the electronic manifold, altering its band structure, including effective mass enhancement. There are, however, cases where such deformations are small, or even if not small, they might couple only weakly to the electronic states that form the band edges, i.e., small deformation potentials, leading to small or negligible mass enhancement. We next illustrate two such examples.

L1 SrBiO₃ (cubic, no rotation, no disproportionation)



L2 SrBiO₃ (monoclinic, has rotation, no disproportionation)



L3 SrBiO₃ (monoclinic, has rotation, has disproportionation)

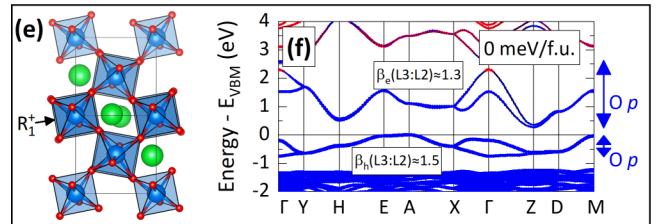


FIG. 9. Mass enhancements in SrBiO₃. (a) The atomic structure and (b) the band structure from the $Pm\bar{3}m$ phase (level 1, L1). The system is metallic and has a broad O p band [blue arrow on the right side of (b)]. (c) The atomic structure and (d) the band structure when allowing the observed (monoclinic) octahedral rotations, but no disproportionate R_1^+ distortion (level 2, L2), where the O p bands become more compact, but the system stays metallic. (e) The atomic structure and (f) the band structure when allowing all experimentally observed distortions (level 3, L3), which leads to the O p bands splitting and, hence, a band gap opening. The R_1^+ distortion can be seen by the slightly different octahedral volumes in (e) (black arrow). Red and blue circle symbols in (b), (d), and (f) denote the orbital projections of Bi p and O p orbitals, respectively; other orbitals are not shown here; the size of the circle is proportional to the composition of orbital. Mass enhancements in (f) with respect to (d), i.e., $\beta(L3 : L2)$, are calculated via the bandwidths of O p bands, which give $\beta_e = 1.3 \pm 0.2$ and $\beta_h = 1.5 \pm 0.2$; the uncertainty is because bandwidths along different \mathbf{k} paths give different enhancement factors. The same PBE functional with spin-orbit coupling has been applied for all SrBiO₃ calculations.

A. Weak octahedral rotations in intrinsic SrTiO₃ cause negligible mass enhancement

Undoped SrTiO₃ is a NM insulator. Positional distortions, such as the octahedral tilting in SrTiO₃ [also known as the antiferrodistortive displacement (AFD)], have been noted in the low-symmetry tetragonal phase [107–109] but are absent in the cubic phase [109–112]. Some observations of distortion in the cubic phase were then attributed to extrinsic factors

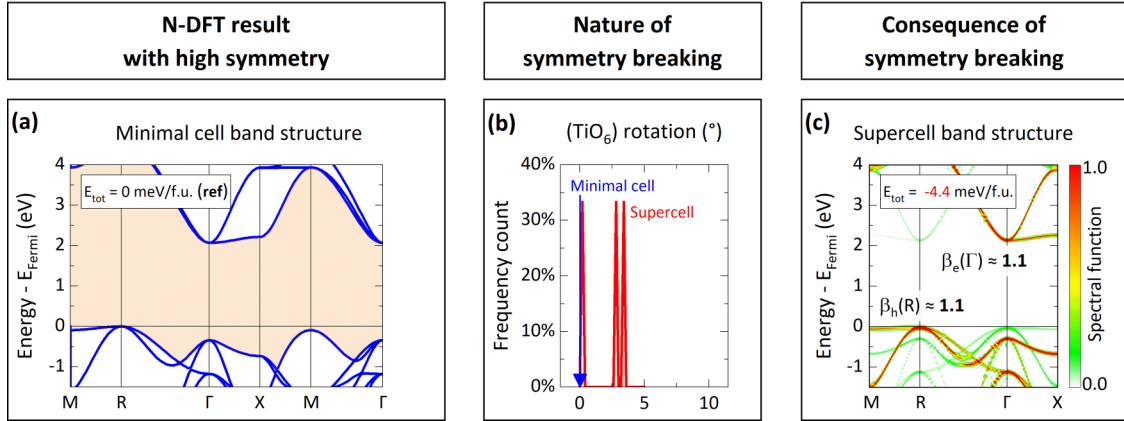
SrTiO₃ (nonmagnetic cubic phase, undoped, SCAN)


FIG. 10. Mass enhancement in the nonmagnetic cubic phase of SrTiO₃. (a) The band structure from the same naïve density functional theory (N-DFT) restriction as in previous literature [110–112], namely a single-cell, cubic, nonmagnetic (NM) SrTiO₃ model, using the SCAN functional. (b) The distribution of octahedral rotation angles. The blue arrow in (b) shows that, in the minimal-cell model, all octahedra have zero rotation, while the red curve shows that, in the supercell, different octahedra have a distribution of tiny rotations around 3–4°. (c) The unfolded band structure when removing the minimal-cell restrictions by using instead a cubic, 64 f.u. NM supercell SrTiO₃ with the same SCAN method. Masses in (c) are calculated via the second derivative of E vs \mathbf{k} , which gives $\beta_e \approx 1.1$ and $\beta_h \approx 1.1$.

such as strain [113–116], defects [117], impurities [118], interface [119], or thermal effect [120]. Indeed, AFD is not expected theoretically in the cubic phase unless one abandons the conventional single f.u. monomorphous description of the $Pm\bar{3}m$ XRD model and allows tilting degree of freedom in a supercell description of the cubic phase. As Table I indicates, here, we focus on the properties of the cubic phase, not the low-temperature ground state, performing a minimization of the cubically constrained total energy as a function of the cell internal atomic positions.

When doped n-type, e.g., SrTiO₃:Nb or SrTiO₃:La at doping concentration of 0.01–0.05 electron/f.u., one observes (i) the formation of a low dispersion (heavy mass) occupied in gap states [121–123], as well as (ii) a Fermi level inside the broad (light mass) principal conduction band. Using plasma frequency as a measure for electron mass $\omega^2 = n_c/m^*$, where n_c is the free carrier concentration, large values of electron mass enhancement of $\beta_e = 2-3$ [73] were reported. We find that, even if removing the single-cell restrictions used in previous studies [i.e., $Pm\bar{3}m$ minimal cell with a single f.u., as shown in Fig. 10(a)] by constructing a supercell (here, 64 f.u.) and relaxing all internal atomic positions, the cubic phase SrTiO₃ shows only small octahedral rotations around 3–4° [shown in Fig. 10(b)], a small total energy lowering of -4.4 meV/f.u., and negligible enhancements for both electron and hole masses [Fig. 10(c); $\beta_e \approx 1.1$ and $\beta_h \approx 1.1$, both calculated from the second derivative of E vs \mathbf{k}]. Thus, our calculated value pertaining to the principal conduction band (not in-gap polaronlike state) $\beta_e \approx 1.1$ indicates negligible enhancement. In the doping concentration 0.05 electron/f.u., both DMFT [110] and N-DFT [110] calculations predict similar electron mass, indicating no mass enhancement by strong electron correlations. It is not clear if the observed substantial electron mass enhancement is related to the presence of polaron states [(i) above] or is intrinsic [(ii) above, due to electron doping [117,118,124] of the main conduction band]. Indeed, the plasma frequency mass enhancement

$\beta = \omega_{\text{model}}^2/\omega_{\text{exp}}^2$ may be affected by doping compensation, reducing the effective concentration of free carriers. The experimental values of mass enhancement in SrTiO₃ appear to require clarification.

B. Antiferroelectric and paraelectric displacements in BaTiO₃ have negligible effects on masses

Another well-known case where local atomic displacement occur involves ferroelectric (FE) compounds, often having paraelectric (PE) and antiferroelectric (AFE) phases. BaTiO₃ is one of the FE perovskite compounds [125–127] where the ferroelectricity is induced by the off-center displacement of the Ti atom in (TiO₆) octahedron. BaTiO₃ experiences a complex phase transition, from rhombohedral (<180 K) to orthorhombic (<280 K) to tetragonal (<400 K) to cubic [128]. While its rhombohedral, orthorhombic, and tetragonal phases all show ferroelectricity, the high-temperature cubic phase shows no net ferroelectricity. Therefore, it has been argued that such a cubic phase has no Ti atom off-center displacement in any octahedra [i.e., a nonelectric (NE) phase] and can be represented by a minimal cubic cell model [129–131]. However, recent investigations show that such a minimal-cell, NE cubic model cannot explain the Raman and x-ray fine structure observations, and the cubic phase could be instead an AFE [44] or PE phase [132]. Here, we aim to study if the AFE and PE nature in cubic BaTiO₃ can have effects on its electronic properties, such as band gap and effective mass.

The AFE phase is mimicked by an 8 f.u. supercell, constraining its lattice vectors to the macroscopically observed cubic structure while relaxing all cell-internal atoms. Figure 11(a) shows the band structure of the NE model (single f.u., NE cubic model) using the SCAN functional. The difference between the atomic positions in the NE monomorphous model and the AFE polymorphous supercell is plotted in Fig. 11(b): the monomorphous cell has no Ti-atom displacement ($\Delta R_i = 0$ for every Ti), while the AFE supercell

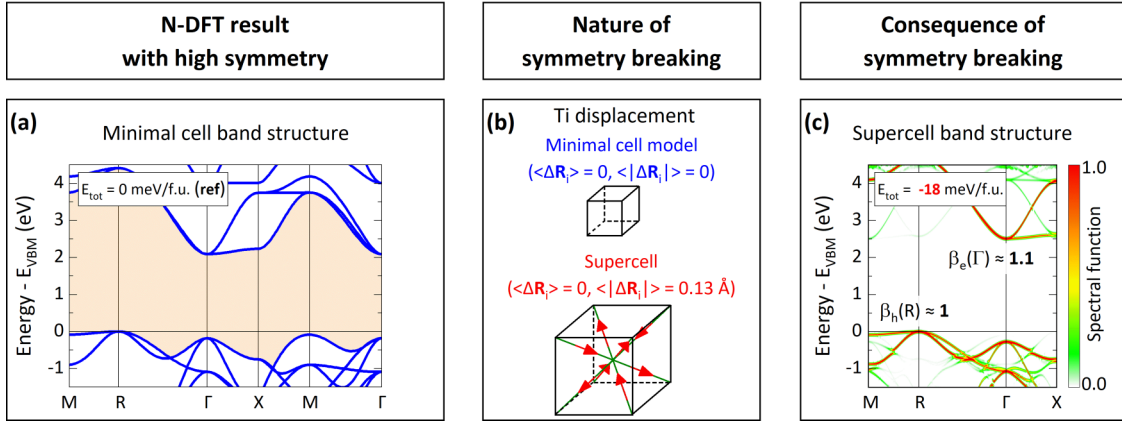
BaTiO₃ (anti-ferroelectric cubic phase, SCAN)

FIG. 11. Mass enhancements in antiferroelectric (AFE) cubic phase of BaTiO₃. (a) The band structure from the same naive density functional theory (N-DFT) restriction as in previous literature [129–131], namely a single-cell, no Ti-atom displacement model, using SCAN functional. (b) The distribution of Ti-atom displacement symmetry breaking: upper part in (b) shows that the minimal-cell model BaTiO₃ does not have any Ti-atom displacement ($\Delta \mathbf{R} = 0$ for each Ti atom), while the lower part in (b) shows that the AFE supercell (8 f.u.) has a unique displacement pattern, where the eight Ti atoms move along eight $\langle 111 \rangle$ directions. In the AFE supercell, the net polarization is zero ($\langle \Delta \mathbf{R} \rangle = 0$), but the local polarization on each Ti site is large ($\langle |\Delta \mathbf{R}_i| \rangle = 0.13 \text{ \AA}$). (c) The unfolded band structure of the 8 f.u. AFE supercell BaTiO₃ with the same SCAN method. Masses in (c) are calculated via the second derivative of E vs \mathbf{k} , which gives $\beta_e \approx 1.1$ and $\beta_h \approx 1$.

shows a unique displacement pattern, where the eight Ti atoms move along the eight $\langle 111 \rangle$ directions (i.e., $[111]$, $[1\bar{1}\bar{1}]$, $[1\bar{1}1]$, $[\bar{1}11]$, $[\bar{1}\bar{1}\bar{1}]$, $[\bar{1}1\bar{1}]$, $[\bar{1}\bar{1}1]$, $[11\bar{1}]$, ...); although the AFE supercell has a zero net polarization ($\langle \Delta \mathbf{R} \rangle = 0$), and the local polarization on each Ti site is nonzero and as large as 0.13 \AA ($\langle |\Delta \mathbf{R}_i| \rangle = 0.13 \text{ \AA}$). Other distortions (rotations, Jahn-Teller distortion, etc.) have all been found to be negligible in the AFE supercell. This AFE displacement pattern agrees well with the previous theory [44]. Figure 11(c) shows the unfolded band structure of the AFE supercell. We found that, although the AFE displacement is large, the mass enhancement is still negligible ($\beta_e \approx 1.1$ and $\beta_h \approx 1$); in other words, the electronic response to such displacements (deformation potential) must be small.

This weak response of band-edge states to Ti off-center displacement can be understood by considering the symmetry mismatch between the orbitals making up the VBM and CBM and the symmetry of the Ti displacement mode: in the cubic primitive cell of BaTiO₃ (NE single f.u. model without displacements or tilting), the system has the space group of $Pm\bar{3}m$, where according to the molecular orbital theory for octahedral O_h symmetry [133], the CBM is pure Ti d orbital (irreducible representation T_{2g}), and the VBM is made up by O $2p$ + Ti $4p$ orbitals (irreducible representation T_{1u}). Considering that the Ti $4p$ orbital is very high in energy, the VBM is almost pure O p (T_{1u}). On the other hand, our supercell model of the AFE state has a large M_2^- distortion mode due to Ti displacements (amplitude = 0.13 \AA , irreducible representation B_{1u} for D_{4h} symmetry), whereas tilting and rotation amplitudes are all smaller than $6 \times 10^{-4} \text{ \AA}$. Since the VBM and CBM are not B_{1u} symmetric, they do not respond to the Ti displacements; thus, the AFE supercell only shows negligible mass enhancement for these states.

The PE phase has been modeled by a 32 f.u. supercell. After the atomic relaxation, all Ti atoms have developed nonzero, nonuniformed local polarizations, as shown by the red curve in Fig. 12(b). The Ti displacement forms a distribution not

only on amplitude but also on directions. We note that the net displacement (vector summation of all Ti displacements) is not zero (0.1 \AA per f.u.) because we do not force any net-polarization condition during the supercell relaxation, and the supercell is in fact weak FE. Nevertheless, the nature of a distribution of static (nonthermal), different displacement in the supercell is by itself different than the low-temperature FE phase. Solving the band structure and doing band unfolding [Fig. 12(c)] shows small mass enhancement of $\beta_e \approx 1.1$ and $\beta_h \approx 1$. The results of both AFE and PE seem consistent in that the coupling of polarization to VBM and CBM states is weak, illustrating cases that the FE displacement has a negligible effect on mass enhancement.

VI. CONCLUSIONS

Symmetry-breaking DFT captures many of the mass enhancement effects previously attributed exclusively to strong electronic correlations under restricted symmetry. Whereas the theoretical methodology of supercell DFT has surely been used in previous studies on many different effects [26], the insights that mass enhancement can be described by mean-field DFT with broken symmetries rather than exclusively by symmetry-restricted many-body approach is noteworthy. The current study further provides a general and intuitive explanation for the physical origins of mass enhancement, as summarized in Fig. 1, including spin symmetry-broken and positional symmetry-broken effects. There are cases where the coupling of distortions to the electronic states at band edges are weak, causing negligible mass renormalization (e.g., SrTiO₃ where the distortion is small, or BaTiO₃ where only Ti displacement, not tilting, lowers the total energy), yet other cases where the distortions and their coupling are strong, leading to large enhancement factors (e.g., SrVO₃, CsPbI₃, LaMnO₃, SrBiO₃), even by the single-determinant mean-field DFT method, which sometimes are even comparable with the

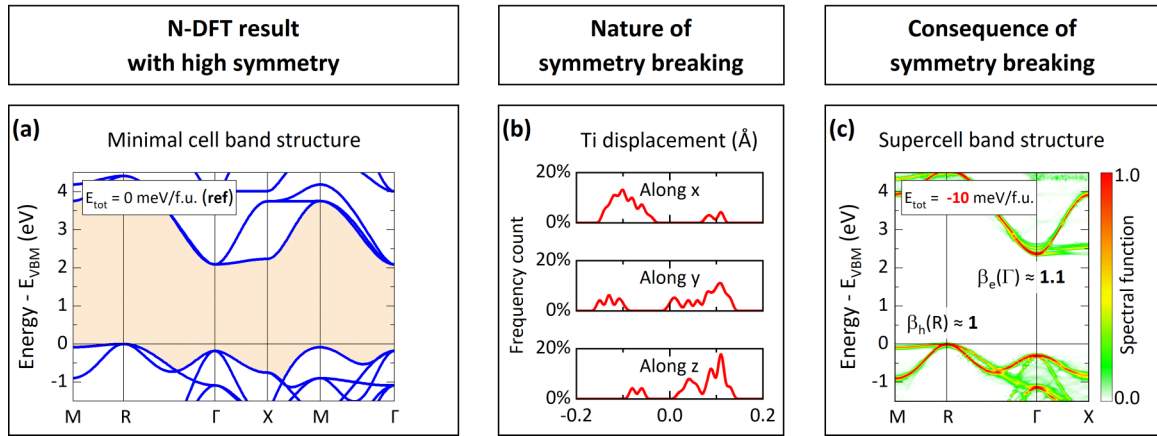
BaTiO₃ (paraelectric cubic phase, SCAN)


FIG. 12. Mass enhancements in the paraelectric (PE) cubic phase of BaTiO₃. (a) The band structure from the same naïve density functional theory (N-DFT) restriction as in previous literature [129–131], identical to Fig. 11(a). (b) The distribution of Ti-atom displacements in the 32 f.u. PE supercell after atomic relaxation along *x*, *y*, and *z* directions ([100], [010], and [001] directions). (c) The unfolded band structure of the 32 f.u. PE supercell BaTiO₃ with the same SCAN method. Masses in (c) are calculated via the second derivative of *E* vs *k*, which gives $\beta_e \approx 1.1$ and $\beta_h \approx 1$.

mass enhancement suggested by the high-order dynamical electron-electron correlation theory. The presence of mass enhancement in the considered systems is not necessarily evidence for the exclusive need for strong dynamically correlated methodologies [15–24].

In principle, the spin fluctuations in a nonvibrating lattice can be either (i) longitudinal (single-site spin flip or intersite spin hopping) or (ii) transversal (single-site spin rotation or spin-wave excitation). The longitudinal fluctuations can be rather fast, e.g., a few femtoseconds, in a metallic system, but slow and very rare in insulators due to the large energy cost of overcoming the band gap. The transversal fluctuations, on the other hand, are typically much slower but not significantly dependent on the metallicity, e.g., in the ordered magnetic ground state of Fe, Ni, and Co, the spin-wave excitations evolve within 1 ps [134], while in the PM state of the small-gap semiconductor CrN, individual moments rotate with respect to its neighbors in the time scale of 50–100 fs [135]. Since ARPES measurement can be done in a time scale of femtoseconds [136], spin fluctuation effects longer than this time scale (longitudinal ones in insulators and transversal ones in both insulators and metals) will be measured as the time average over many properties of individual spin configurations (average of the properties), while spin fluctuation effects shorter than a few femtoseconds (longitudinal ones in some metals) will be observed as the properties of a time-averaged spin configuration (property of the average).

For the PM phase, in a symmetry-restricted many-body approach (a) containing a single magnetic moment (monomorphous limit) interacting with an average bath, the magnetic moment must fluctuate in time to conserve the zero total moment expected of a paramagnet. In a symmetry-broken representation (b) containing a polymorphous distribution of many local moments, as used in this paper, the orientation of the moment is static, but there are many orientations resolved spatially. In both cases (a) and (b), the average moment is zero (time average in symmetry-restricted approach and spatial average in symmetry-broken approach) as required of the

PM state, while by ergodicity, the symmetry-broken approach with static, spatial distribution of individual moments can reproduce the ARPES observation if the spin fluctuations are longer than a few femtoseconds (e.g., longitudinal ones in insulators and transversal ones in both insulators and metals).

ACKNOWLEDGMENTS

The work at the University of Colorado at Boulder was supported by the U.S. Department of Energy, Office of Science, Basic Energy Sciences, Materials Sciences and Engineering Division under Grant No. DE-SC0010467 to the University of Colorado. The *ab initio* calculations in this paper were performed using resources of the National Energy Research Scientific Computing Center, which is supported by the Office of Science of the U.S. Department of Energy.

APPENDIX A: DFT DETAILS

To calculate the total energy, band structure, and effective mass, the plane-wave pseudopotential DFT method, as implemented in the VASP software package [137,138] has been used. (i) For transition metal oxides with localized orbitals SrTiO₃, BaTiO₃, and LaMnO₃, the SCAN functional [139], used previously [99,140] has been applied. (ii) For metallic SrVO₃, the SCAN functional could not reach a self-converged charge density in our large PM cubic supercell (640 atom/f.u.); therefore, for all SrVO₃ cells, the PBE functional + *U* (with *U* = 1.25 eV on *V d* orbitals) used previously [27] has been applied instead. Figure 13 shows the difference of DOS between the SCAN and PBE + *U* DFT results for a smaller 320 atom supercell of PM cubic phase SrVO₃. It can be seen from Fig. 13 that the PBE + *U* and SCAN functionals give (1) very similar DOS at Fermi level and (2) very similar bandwidths; they, therefore, should predict very similar mass enhancement factors. (iii) The *s-p*-bonded halide CsPbI₃ has been calculated using the

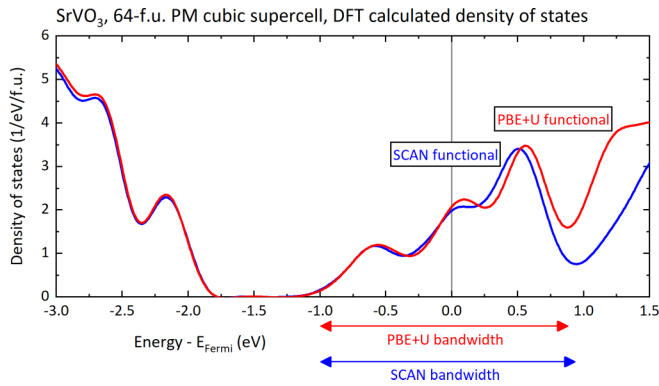


FIG. 13. Comparison of density of states (DOS) from density functional theory (DFT) calculations using PBE + U (red curve) and SCAN (blue curve) functionals for the 64 f.u. (320 atom) paramagnetic (PM) cubic supercell of SrVO₃. The two functionals show remarkably similar DOS at Fermi level and very similar bandwidths (denoted by the red and blue arrows).

PBE functional. Note that no SOC has been considered for CsPbI₃ in this paper because the PBE functional will give too small a gap (~ 0.1 eV) if applied together with SOC; a better agreement with experimentally observed gap can be achieved by using SOC with a hybrid functional such as Heyd-Scuseria-Ernzerhof, which is however beyond the scope of this paper. (iv) The s - p -bonded oxide SrBiO₃ has been calculated using the PBE with SOC effect.

For each compound, we have applied the DFT lattice constants obtained from the minimal cell model to all supercell calculations: $a = 3.83$ Å (cubic SrVO₃); $a = 6.27$ Å (cubic CsPbI₃); $a = 5.51$ Å, $b = 5.81$ Å, and $c = 7.64$ Å (LaMnO₃ with Jahn-Teller-like distortion); $a = 5.57$ Å and $c = 7.87$ Å (LaMnO₃ without Jahn-Teller distortion); $a = 6.01$ Å, $b = 6.20$ Å, and $c = 10.49$ Å (monoclinic SrBiO₃); $a = 4.52$ Å (cubic SrBiO₃); $a = 3.91$ Å (cubic SrTiO₃); and $a = 4.03$ Å (cubic BaTiO₃). To minimize the numerical error, for all cells of the same compound in the same phase (e.g., SrVO₃ single f.u. cubic primitive cell vs SrVO₃ 64 f.u. cubic supercell),

TABLE II. Summary of DFT total energy for different collinear magnetic structures of cubic SrVO₃. The same PBE + U method has been applied for all SrVO₃ calculations. All structures have the same lattice constant and atomic positions and only differ in the way up- and down-spin moments occupy vanadium sites. Magnetic orders NM, FM, AFM (G-type and A-type), and PM denote non-magnetic, ferromagnetic, antiferromagnetic, and paramagnetic (from SQS method), respectively. The DFT total energy of the NM phase has been chosen as the reference (0 eV).

Cubic SrVO ₃ magnetic phase	Total energy (meV/f.u.)
NM (1 f.u.)	0 (reference)
FM (1 f.u.)	-15
AFM-G (8 f.u.)	-31
AFM-A (2 f.u.)	-26
PM (64 f.u.)	-30
PM (128 f.u.)	-31

their total energies are calculated using an uniformed energy cutoff for the plane-wave basis set, a uniformed tolerance for total energy convergence (10^{-8} eV/atom), and an equivalent set of k -point sampling in BZ for every cell (equivalent to a $12 \times 12 \times 12$ Γ -centered k -mesh in the primitive BZ).

APPENDIX B: MAGNETIC STRUCTURE OF SrVO₃

Table II summarizes the DFT total energies of different magnetic orders of cubic SrVO₃: NM = nonmagnetic, FM = ferromagnetic, AFM-G = G-type antiferromagnetic, AFM-A = A-type antiferromagnetic, and PM = collinear paramagnetic phase from SQS method. All magnetic structures show more significant energy lowering than the NM model, but very similar total energy with each other. The results agree with the experimental observation that SrVO₃ shows no magnetic order down to $T = 0$ K.

[1] C. Kittel, *Introduction to Solid State Physics* (Wiley, New York, 1966).
 [2] M. Yi, Y. Zhang, Z.-X. Shen, and D. Lu, Role of the orbital degree of freedom in iron-based superconductors, *Npj Quantum Mater.* **2**, 57 (2017).
 [3] Y. S. Kushnirenko, A. A. Kordyuk, A. V. Fedorov, E. Haubold, T. Wolf, B. Büchner, and S. V. Borisenko, Anomalous temperature evolution of the electronic structure of FeSe, *Phys. Rev. B* **96**, 100504(R) (2017).
 [4] M. Schlipf, S. Poncé, and F. Giustino, Carrier Lifetimes and Polaronic Mass Enhancement in the Hybrid Halide Perovskite CH₃NH₃PbI₃ from Multiphonon Fröhlich Coupling, *Phys. Rev. Lett.* **121**, 086402 (2018).
 [5] C. Verdi, F. Caruso, and F. Giustino, Origin of the crossover from polarons to Fermi liquids in transition metal oxides, *Nat. Commun.* **8**, 1 (2017).

[6] Y. Okada, T. Arima, Y. Tokura, C. Murayama, and N. Mōri, Doping- and pressure-induced change of electrical and magnetic properties in the Mott-Hubbard insulator LaTiO₃, *Phys. Rev. B* **48**, 9677 (1993).
 [7] J.-J. Zhou, O. Hellman, and M. Bernardi, Electron-Phonon Scattering in the Presence of Soft Modes and Electron Mobility in SrTiO₃ Perovskite from First Principles, *Phys. Rev. Lett.* **121**, 226603 (2018).
 [8] D. E. Shai, C. Adamo, D. W. Shen, C. M. Brooks, J. W. Harter, E. J. Monkman, B. Burganov, D. G. Schlom, and K. M. Shen, Quasiparticle Mass Enhancement and Temperature Dependence of the Electronic Structure of Ferromagnetic SrRuO₃ Thin Films, *Phys. Rev. Lett.* **110**, 087004 (2013).
 [9] T. M. Rice and M. Sigrist, Sr₂RuO₄: An electronic analogue of ³He? *J. Phys. Condens. Matter* **7**, L643 (1995).

- [10] P. B. Allen, H. Berger, O. Chauvet, L. Forro, T. Jarlborg, A. Junod, B. Revaz, and G. Santi, Transport properties, thermodynamic properties, and electronic structure of SrRuO₃, *Phys. Rev. B* **53**, 4393 (1996).
- [11] I. H. Inoue, O. Goto, H. Makino, N. E. Hussey, and M. Ishikawa, Bandwidth control in a perovskite-type 3d¹-correlated metal Ca_{1-x}Sr_xVO₃ I. Evolution of the electronic properties and effective mass, *Phys. Rev. B* **58**, 4372 (1998).
- [12] T. Yoshida, M. Hashimoto, T. Takizawa, A. Fujimori, M. Kubota, K. Ono, and H. Eisaki, Mass renormalization in the bandwidth-controlled Mott-Hubbard systems SrVO₃ and CaVO₃ studied by angle-resolved photoemission spectroscopy, *Phys. Rev. B* **82**, 085119 (2010).
- [13] T. Yoshida, K. Tanaka, H. Yagi, A. Ino, H. Eisaki, A. Fujimori, and Z.-X. Shen, Direct Observation of the Mass Renormalization in SrVO₃ by Angle Resolved Photoemission Spectroscopy, *Phys. Rev. Lett.* **95**, 146404 (2005).
- [14] T. Yoshida, M. Kobayashi, K. Yoshimatsu, H. Kumigashira, and A. Fujimori, Correlated electronic states of SrVO₃ revealed by angle-resolved photoemission spectroscopy, *J. Electron Spectrosc. Relat. Phenom.* **208**, 11 (2016).
- [15] I. A. Nekrasov, K. Held, G. Keller, D. E. Kondakov, Th. Pruschke, M. Kollar, O. K. Andersen, V. I. Anisimov, and D. Vollhardt, Momentum-resolved spectral functions of SrVO₃ calculated by LDA + DMFT, *Phys. Rev. B* **73**, 155112 (2006).
- [16] J. M. Tomczak, M. Casula, T. Miyake, and S. Biermann, Asymmetry in band widening and quasiparticle lifetimes in SrVO₃: Competition between screened exchange and local correlations from combined GW and dynamical mean-field theory GW + DMFT, *Phys. Rev. B* **90**, 165138 (2014).
- [17] R. Sakuma, Ph. Werner, and F. Aryasetiawan, Electronic structure of SrVO₃ within GW + DMFT, *Phys. Rev. B* **88**, 235110 (2013).
- [18] E. Pavarini, S. Biermann, A. Poteryaev, A. I. Lichtenstein, A. Georges, and O. K. Andersen, Mott Transition and Suppression of Orbital Fluctuations in Orthorhombic 3d¹ Perovskites, *Phys. Rev. Lett.* **92**, 176403 (2004).
- [19] X. Deng, K. Haule, and G. Kotliar, Transport Properties of Metallic Ruthenates: A DFT + DMFT Investigation, *Phys. Rev. Lett.* **116**, 256401 (2016).
- [20] E. Jakobi, S. Kanungo, S. Sarkar, S. Schmitt, and T. Saha-Dasgupta, LDA+DMFT study of Ru-based perovskite SrRuO₃ and CaRuO₃, *Phys. Rev. B* **83**, 041103(R) (2011).
- [21] S. L. Skornyakov, N. A. Skorikov, A. V. Lukoyanov, A. O. Shorikov, and V. I. Anisimov, LDA+DMFT spectral functions and effective electron mass enhancement in the superconductor LaFePO, *Phys. Rev. B* **81**, 174522 (2010).
- [22] E. A. Nowadnick, J. P. Ruf, H. Park, P. D. C. King, D. G. Schlom, K. M. Shen, and A. J. Millis, Quantifying electronic correlation strength in a complex oxide: A combined DMFT and ARPES study of LaNiO₃, *Phys. Rev. B* **92**, 245109 (2015).
- [23] Z. P. Yin, K. Haule, and G. Kotliar, Kinetic frustration and the nature of the magnetic and paramagnetic states in iron pnictides and iron chalcogenides, *Nat. Mater.* **10**, 932 (2011).
- [24] J. Mravlje, M. Aichhorn, T. Miyake, K. Haule, G. Kotliar, and A. Georges, Coherence-Incoherence Crossover and the Mass-Renormalization Puzzles in Sr₂RuO₄, *Phys. Rev. Lett.* **106**, 096401 (2011).
- [25] J. M. Tomczak, M. van Schilfgaarde, and G. Kotliar, Many-Body Effects in Iron Pnictides and Chalcogenides: Nonlocal Versus Dynamic Origin of Effective Masses, *Phys. Rev. Lett.* **109**, 237010 (2012).
- [26] G. Trimarchi, Z. Wang, and A. Zunger, Polymorphous band structure model of gapping in the antiferromagnetic and paramagnetic phases of the Mott insulators MnO, FeO, CoO, and NiO, *Phys. Rev. B* **97**, 035107 (2018).
- [27] J. Varignon, M. Bibes, and A. Zunger, Origin of band gaps in 3d perovskite oxides, *Nat. Commun.* **10**, 1658 (2019).
- [28] O. I. Malyi, G. M. Dalpian, X.-G. Zhao, Z. Wang, and A. Zunger, Realization of predicted exotic materials: The burden of proof, *Mater. Today* **32**, 35 (2020).
- [29] O. I. Malyi and A. Zunger, False metals, real insulators, and degenerate gapped metals, *Appl. Phys. Rev.* **7**, 041310 (2020).
- [30] M. R. Filip, G. E. Eperon, H. J. Snaith, and F. Giustino, Steric engineering of metal-halide perovskites with tunable optical band gaps, *Nat. Commun.* **5**, 1 (2014).
- [31] J. Even and C. Katan, *Ab initio* and first principles studies of halide perovskites, in *Halide Perovskites*, edited by T.-C. Sum and N. Mathews (Wiley, Weinheim, 2018).
- [32] D. H. Fabini, G. Laurita, J. S. Bechtel, C. C. Stoumpos, H. A. Evans, A. G. Kontos, Y. S. Raptis, P. Falaras, A. Van der Ven, and M. G. Kanatzidis, Dynamic stereochemical activity of the Sn²⁺ lone pair in perovskite CsSnBr₃, *J. Am. Chem. Soc.* **138**, 11820 (2016).
- [33] S. Chakraborty, W. Xie, N. Mathews, M. Sherburne, R. Ahuja, M. Asta, and S. G. Mhaisalkar, Rational design: A high-throughput computational screening and experimental validation methodology for lead-free and emergent hybrid perovskites, *ACS Energy Lett.* **2**, 837 (2017).
- [34] E. S. Božin, C. D. Malliakas, P. Souvatzis, T. Proffen, N. A. Spaldin, M. G. Kanatzidis, and S. J. L. Billinge, Entropically stabilized local dipole formation in lead chalcogenides, *Science* **330**, 1660 (2010).
- [35] A. N. Beecher, O. E. Semonin, J. M. Skelton, J. M. Frost, M. W. Terban, H. Zhai, A. Alatas, J. S. Owen, A. Walsh, and S. J. L. Billinge, Direct observation of dynamic symmetry breaking above room temperature in methylammonium lead iodide perovskite, *ACS Energy Lett.* **1**, 880 (2016).
- [36] X. Zhao, G. M. Dalpian, Z. Wang, and A. Zunger, Polymorphous nature of cubic halide perovskites, *Phys. Rev. B* **101**, 155137 (2020).
- [37] I.-K. Jeong, T. W. Darling, J. K. Lee, Th. Proffen, R. H. Heffner, J. S. Park, K. S. Hong, W. Dmowski, and T. Egami, Direct Observation of the Formation of Polar Nanoregions in Pb(Mg_{1/3}Nb_{2/3})O₃ Using Neutron Pair Distribution Function Analysis, *Phys. Rev. Lett.* **94**, 147602 (2005).
- [38] E. S. Bozin, W. G. Yin, R. J. Koch, M. Abeykoon, Y. S. Hor, H. Zheng, H. C. Lei, C. Petrovic, J. F. Mitchell, and S. J. L. Billinge, Local orbital degeneracy lifting as a precursor to an orbital-selective Peierls transition, *Nat. Commun.* **10**, 1 (2019).
- [39] T. Egami and S. J. Billinge, *Underneath the Bragg Peaks: Structural Analysis of Complex Materials*, 2nd ed. (Elsevier, Amsterdam, 2012).
- [40] J. J. Rehr and R. C. Albers, Theoretical approaches to x-ray absorption fine structure, *Rev. Mod. Phys.* **72**, 621 (2000).
- [41] J. C. Mikkelsen Jr and J. B. Boyce, Atomic-Scale Structure of Random Solid Solutions: Extended X-Ray-Absorption Fine-Structure Study of Ga_{1-x}In_xAs, *Phys. Rev. Lett.* **49**, 1412 (1982).

- [42] A. Bianconi, N. L. Saini, A. Lanzara, M. Missori, T. Rossetti, H. Oyanagi, H. Yamaguchi, K. Oka, and T. Ito, Determination of the Local Lattice Distortions in the CuO_2 Plane of $\text{La}_{1.85}\text{Sr}_{0.15}\text{CuO}_4$, *Phys. Rev. Lett.* **76**, 3412 (1996).
- [43] A. M. Glazer, The classification of tilted octahedra in perovskites, *Acta Crystallogr. B* **28**, 3384 (1972).
- [44] Q. Zhang, T. Cagin, and W. A. Goddard, The ferroelectric and cubic phases in BaTiO_3 ferroelectrics are also antiferroelectric, *Proc. Natl. Acad. Sci.* **103**, 14695 (2006).
- [45] J. A. Alonso, J. L. García-Muñoz, M. T. Fernández-Díaz, M. A. G. Aranda, M. J. Martínez-Lope, and M. T. Casais, Charge Disproportionation in RNiO_3 Perovskites: Simultaneous Metal-Insulator and Structural Transition in YNiO_3 , *Phys. Rev. Lett.* **82**, 3871 (1999).
- [46] J. A. Alonso, M. J. Martínez-Lope, M. T. Casais, and M. T. Fernández-Díaz, Evolution of the Jahn-Teller distortion of MnO_6 octahedra in RMnO_3 perovskites ($R = \text{Pr, Nd, Dy, Tb, Ho, Er, Y}$): A neutron diffraction study, *Inorg. Chem.* **39**, 917 (2000).
- [47] R. Prasanna, A. Gold-Parker, T. Leijtens, B. Conings, A. Babayigit, H.-G. Boyen, M. F. Toney, and M. D. McGehee, Band gap tuning via lattice contraction and octahedral tilting in perovskite materials for photovoltaics, *J. Am. Chem. Soc.* **139**, 11117 (2017).
- [48] Z. Gui, L.-W. Wang, and L. Bellaiche, Electronic properties of electrical vortices in ferroelectric nanocomposites from large-scale *ab initio* computations, *Nano Lett.* **15**, 3224 (2015).
- [49] K. Foyevtsova, A. Khazraie, I. Elfimov, and G. A. Sawatzky, Hybridization effects and bond disproportionation in the bismuth perovskites, *Phys. Rev. B* **91**, 121114(R) (2015).
- [50] N. Balke, B. Winchester, W. Ren, Y. H. Chu, A. N. Morozovska, E. A. Eliseev, M. Huijben, R. K. Vasudevan, P. Maksymovych, J. Britson, S. Jesse, I. Kornev, R. Ramesh, L. Bellaiche, L. Q. Chen, and S. V. Kalinin, Enhanced electric conductivity at ferroelectric vortex cores in BiFeO_3 , *Nat. Phys.* **8**, 81 (2012).
- [51] A. Mercy, J. Bieder, J. Íñiguez, and P. Ghosez, Structurally triggered metal-insulator transition in rare-earth nickelates, *Nat. Commun.* **8**, 1 (2017).
- [52] A. Amat, E. Mosconi, E. Ronca, C. Quarti, P. Umari, Md. K. Nazeeruddin, M. Grätzel, and F. De Angelis, Cation-induced band-gap tuning in organohalide perovskites: Interplay of spin-orbit coupling and octahedra tilting, *Nano Lett.* **14**, 3608 (2014).
- [53] I. Leonov, Dm. Korotin, N. Binggeli, V. I. Anisimov, and D. Vollhardt, Computation of correlation-induced atomic displacements and structural transformations in paramagnetic KCuF_3 and LaMnO_3 , *Phys. Rev. B* **81**, 075109 (2010).
- [54] X. Wang, M. J. Han, L. de' Medici, H. Park, C. A. Marianetti, and A. J. Millis, Covalency, double-counting, and the metal-insulator phase diagram in transition metal oxides, *Phys. Rev. B* **86**, 195136 (2012).
- [55] M. De Raychaudhury, E. Pavarini, and O. K. Andersen, Orbital Fluctuations in the Different Phases of LaVO_3 and YVO_3 , *Phys. Rev. Lett.* **99**, 126402 (2007).
- [56] Z. Wang, J.-W. Luo, and A. Zunger, Alloy theory with atomic resolution for Rashba or topological systems, *Phys. Rev. Mater.* **3**, 044605 (2019).
- [57] Z. Wang, Q. Liu, J.-W. Luo, and A. Zunger, Digging for topological property in disordered alloys: The emergence of Weyl semimetal phase and sequential band inversions in PbSe-SnSe alloys, *Mater. Horiz.* **6**, 2124 (2019).
- [58] Z. Wang, X.-G. Zhao, R. Koch, S. J. L. Billinge, and A. Zunger, Understanding electronic peculiarities in tetragonal FeSe as local structural symmetry breaking, *Phys. Rev. B* **102**, 235121 (2020).
- [59] J. P. Perdew and A. Zunger, Self-interaction correction to density-functional approximations for many-electron systems, *Phys. Rev. B* **23**, 5048 (1981).
- [60] P. S. Bagus and H. F. Schaefer III, Localized and delocalized $1s$ hole states of the O_2^+ molecular ion, *J. Chem. Phys.* **56**, 224 (1972).
- [61] O. Gunnarsson and B. I. Lundqvist, Exchange and correlation in atoms, molecules, and solids by the spin-density-functional formalism, *Phys. Rev. B* **13**, 4274 (1976).
- [62] M. R. Pederson, R. A. Heaton, and C. C. Lin, Density-functional theory with self-interaction correction: Application to the lithium molecule, *J. Chem. Phys.* **82**, 2688 (1985).
- [63] J. P. Perdew, A. Ruzsinszky, J. Sun, N. K. Nepal, and A. D. Kaplan, Interpretations of ground-state symmetry breaking and strong correlation in wavefunction and density functional theories, *Proc. Natl. Acad. Sci.* **118**, e2017850118 (2021).
- [64] C. Yannouleas and U. Landman, Electronic shell effects in triaxially deformed metal clusters: A systematic interpretation of experimental observations, *Phys. Rev. B* **51**, 1902 (1995).
- [65] F. Herman, Theoretical investigation of the electronic energy band structure of solids, *Rev. Mod. Phys.* **30**, 102 (1958).
- [66] P. Yu and M. Cardona, 2.6: The $\mathbf{k}p$ method of band-structure calculations, in *Fundamentals of Semiconductors: Physics and Materials Properties*, 3rd ed. (Springer-Verlag, Berlin, Heidelberg, 1996).
- [67] A. J. Cohen, P. Mori-Sánchez, and W. Yang, Fractional charge perspective on the band gap in density-functional theory, *Phys. Rev. B* **77**, 115123 (2008).
- [68] P. Mori-Sánchez, A. J. Cohen, and W. Yang, Localization and Delocalization Errors in Density Functional Theory and Implications for Band-Gap Prediction, *Phys. Rev. Lett.* **100**, 146401 (2008).
- [69] J. P. Perdew, W. Yang, K. Burke, Z. Yang, E. K. Gross, M. Scheffler, G. E. Scuseria, T. M. Henderson, I. Y. Zhang, and A. Ruzsinszky, Understanding band gaps of solids in generalized Kohn-Sham theory, *Proc. Natl. Acad. Sci.* **114**, 2801 (2017).
- [70] A. H. Hill, C. L. Kennedy, E. S. Massaro, and E. M. Grumstrup, Perovskite carrier transport: Disentangling the impacts of effective mass and scattering time through microscopic optical detection, *J. Phys. Chem. Lett.* **9**, 2808 (2018).
- [71] M. Takizawa, M. Minohara, H. Kumigashira, D. Toyota, M. Oshima, H. Wadati, T. Yoshida, A. Fujimori, M. Lippmaa, M. Kawasaki, H. Koinuma, G. Sordi, and M. Rozenberg, Coherent and incoherent d band dispersions in SrVO_3 , *Phys. Rev. B* **80**, 235104 (2009).
- [72] A. Chikamatsu, H. Wadati, H. Kumigashira, M. Oshima, A. Fujimori, N. Hamada, T. Ohnishi, M. Lippmaa, K. Ono, and M. Kawasaki, Band structure and Fermi surface of $\text{La}_{0.6}\text{Sr}_{0.4}\text{MnO}_3$ thin films studied by *in situ* angle-resolved photoemission spectroscopy, *Phys. Rev. B* **73**, 195105 (2006).

- [73] J. L. M. van Mechelen, D. van der Marel, C. Grimaldi, A. B. Kuzmenko, N. P. Armitage, N. Reyren, H. Hagemann, and I. I. Mazin, Electron-Phonon Interaction and Charge Carrier Mass Enhancement in SrTiO_3 , *Phys. Rev. Lett.* **100**, 226403 (2008).
- [74] L.-W. Wang, L. Bellaiche, S.-H. Wei, and A. Zunger, Majority Representation of Alloy Electronic States, *Phys. Rev. Lett.* **80**, 4725 (1998).
- [75] V. Popescu and A. Zunger, Effective Band Structure of Random Alloys, *Phys. Rev. Lett.* **104**, 236403 (2010).
- [76] V. Popescu and A. Zunger, Extracting E versus \mathbf{k} effective band structure from supercell calculations on alloys and impurities, *Phys. Rev. B* **85**, 085201 (2012).
- [77] A. Zunger, S.-H. Wei, L. G. Ferreira, and J. E. Bernard, Special Quasirandom Structures, *Phys. Rev. Lett.* **65**, 353 (1990).
- [78] L. Bellaiche and A. Zunger, Effects of atomic short-range order on the electronic and optical properties of GaAsN, GaInN, and GaInAs alloys, *Phys. Rev. B* **57**, 4425 (1998).
- [79] C. Wolverton, V. Ozolins, and A. Zunger, Short-range-order types in binary alloys: A reflection of coherent phase stability, *J. Phys. Condens. Matter* **12**, 2749 (2000).
- [80] B. L. Chamberland and P. S. Danielson, Alkaline-earth vanadium (IV) oxides having the AVO_3 composition, *J. Solid State Chem.* **3**, 243 (1971).
- [81] M. J. Rey, Ph. Dehault, J. C. Joubert, B. Lambert-Andron, M. Cyrot, and F. Cyrot-Lackmann, Preparation and structure of the compounds SrVO_3 and Sr_2VO_4 , *J. Solid State Chem.* **86**, 101 (1990).
- [82] P. Puschnig and D. Lüftner, Simulation of angle-resolved photoemission spectra by approximating the final state by a plane wave: From graphene to polycyclic aromatic hydrocarbon molecules, *J. Electron Spectrosc. Relat. Phenom.* **200**, 193 (2015).
- [83] S. Moser, An experimentalist's guide to the matrix element in angle resolved photoemission, *J. Electron Spectrosc. Relat. Phenom.* **214**, 29 (2017).
- [84] D. E. Eastman, J. A. Knapp, and F. J. Himpsel, Direct Determination of Lifetime and Energy Dispersion for the Empty Δ_1 Conduction Band of Copper, *Phys. Rev. Lett.* **41**, 825 (1978).
- [85] J. A. Knapp, F. J. Himpsel, and D. E. Eastman, Experimental energy band dispersions and lifetimes for valence and conduction bands of copper using angle-resolved photoemission, *Phys. Rev. B* **19**, 4952 (1979).
- [86] I. Stockem, A. Bergman, A. Glensk, T. Hickel, F. Körmann, B. Grabowski, J. Neugebauer, and B. Alling, Anomalous Phonon Lifetime Shortening in Paramagnetic CrN Caused by Spin-Lattice Coupling: A Combined Spin and *Ab Initio* Molecular Dynamics Study, *Phys. Rev. Lett.* **121**, 125902 (2018).
- [87] V. M. Goldschmidt, Die Gesetze der Krystallochemie, *Naturwissenschaften* **14**, 477 (1926).
- [88] X. Qiu, Th. Proffen, J. F. Mitchell, and S. J. L. Billinge, Orbital Correlations in the Pseudocubic O and Rhombohedral R Phases of LaMnO_3 , *Phys. Rev. Lett.* **94**, 177203 (2005).
- [89] P. García-Fernández, S. Ghosh, N. J. English, and J. A. Aramburu, Benchmark study for the application of density functional theory to the prediction of octahedral tilting in perovskites, *Phys. Rev. B* **86**, 144107 (2012).
- [90] J. Even, L. Pedesseau, J.-M. Jancu, and C. Katan, DFT and $\mathbf{k} \cdot \mathbf{p}$ modelling of the phase transitions of lead and tin halide perovskites for photovoltaic cells, *Phys. Status Solidi RRL* **8**, 31 (2014).
- [91] E. Mosconi, P. Umari, and F. D. Angelis, Electronic and optical properties of MAPbX_3 perovskites ($X = \text{I}, \text{Br}, \text{Cl}$): A unified DFT and GW theoretical analysis, *Phys. Chem. Chem. Phys.* **18**, 27158 (2016).
- [92] A. Perrichon, E. Jedvik Granhed, G. Romanelli, A. Piovano, A. Lindman, P. Hyltdgaard, G. Wahnström, and M. Karlsson, Unraveling the ground-state structure of BaZrO_3 by neutron scattering experiments and first-principles calculations, *Chem. Mater.* **32**, 2824 (2020).
- [93] Z. Xiao, W. Meng, J. Wang, D. B. Mitzi, and Y. Yan, Searching for promising new perovskite-based photovoltaic absorbers: The importance of electronic dimensionality, *Mater. Horiz.* **4**, 206 (2017).
- [94] S. C. Miller and W. F. Love, *Tables of Irreducible Representations of Space Groups and Co-Representations of Magnetic Space Groups* (Pruett Press, Boulder, Colorado, 1967).
- [95] E. Pavarini and E. Koch, Origin of Jahn-Teller Distortion and Orbital Order in LaMnO_3 , *Phys. Rev. Lett.* **104**, 086402 (2010).
- [96] S. Satpathy, Z. S. Popović, and F. R. Vukajlović, Electronic Structure of the Perovskite Oxides: $\text{La}_{1-x}\text{Ca}_x\text{MnO}_3$, *Phys. Rev. Lett.* **76**, 960 (1996).
- [97] J. H. Lee, K. T. Delaney, E. Bousquet, N. A. Spaldin, and K. M. Rabe, Strong coupling of Jahn-Teller distortion to oxygen-octahedron rotation and functional properties in epitaxially strained orthorhombic LaMnO_3 , *Phys. Rev. B* **88**, 174426 (2013).
- [98] T. A. Mellan, F. Cora, R. Grau-Crespo, and S. Ismail-Beigi, Importance of anisotropic Coulomb interaction in LaMnO_3 , *Phys. Rev. B* **92**, 085151 (2015).
- [99] J. Varignon, M. Bibes, and A. Zunger, Mott gapping in $3d\text{ABO}_3$ perovskites without Mott-Hubbard interelectronic repulsion energy U , *Phys. Rev. B* **100**, 035119 (2019).
- [100] J. Varignon, M. Bibes, and A. Zunger, Origins versus fingerprints of the Jahn-Teller effect in d -electron ABX_3 perovskites, *Phys. Rev. Res.* **1**, 033131 (2019).
- [101] J. B. Goodenough, Jahn-Teller phenomena in solids, *Annu. Rev. Mater. Sci.* **28**, 1 (1998).
- [102] J. Kuneš, I. Leonov, M. Kollar, K. Byczuk, V. I. Anisimov, and D. Vollhardt, Dynamical mean-field approach to materials with strong electronic correlations, *Eur. Phys. J. Spec. Top.* **180**, 5 (2009).
- [103] H. Banerjee, O. Janson, K. Held, and T. Saha-Dasgupta, Electronic and magnetic state of LaMnO_3 epitaxially strained on SrTiO_3 : Effect of local correlation and nonlocal exchange, *Phys. Rev. B* **100**, 115143 (2019).
- [104] P. V. Balachandran and J. M. Rondinelli, Interplay of octahedral rotations and breathing distortions in charge-ordering perovskite oxides, *Phys. Rev. B* **88**, 054101 (2013).
- [105] G. M. Dalpian, Q. Liu, J. Varignon, M. Bibes, and A. Zunger, Bond Disproportionation, Charge self-regulation, and ligand holes in $s-p$ and in d -electron ABX_3 perovskites by density functional theory, *Phys. Rev. B* **98**, 075135 (2018).
- [106] S. M. Kazakov, C. Chaillout, P. Bordet, J. J. Capponi, M. Nunez-Regueiro, A. Rysak, J. L. Tholence, P. G. Radaelli, S. N. Putilin, and E. V. Antipov, Discovery of a second family of bismuth-oxide-based superconductors, *Nature* **390**, 148 (1997).

- [107] K. Tsuda and M. Tanaka, Refinement of crystal structure parameters using convergent-beam electron diffraction: The low-temperature phase of SrTiO₃, *Acta Crystallogr. A* **51**, 7 (1995).
- [108] Yu. A. Abramov, V. G. Tsirel'son, V. E. Zavodnik, S. A. Ivanov, and I. D. Brown, The chemical bond and atomic displacements in SrTiO₃ from x-ray diffraction analysis, *Acta Crystallogr. B* **51**, 942 (1995).
- [109] K. B. Lyons and P. A. Fleury, Phonon interactions and the dynamic central peak in SrTiO₃ near the structural phase transition, *Solid State Commun.* **23**, 477 (1977).
- [110] A. van Roekeghem and S. Biermann, Screened exchange dynamical mean-field theory and its relation to density functional theory: SrVO₃ and SrTiO₃, *EPL Europhys. Lett.* **108**, 57003 (2014).
- [111] A. F. Santander-Syro, O. Copie, T. Kondo, F. Fortuna, S. Pailhès, R. Weht, X. G. Qiu, F. Bertran, A. Nicolaou, A. Taleb-Ibrahimi, P. Le Fèvre, G. Herranz, M. Bibes, N. Reyren, Y. Apertet, P. Lecoeur, A. Barthélémy, and M. J. Rozenberg, Two-dimensional electron gas with universal subbands at the surface of SrTiO₃, *Nature* **469**, 189 (2011).
- [112] Y. J. Chang, A. Bostwick, Y. S. Kim, K. Horn, and E. Rotenberg, Structure and correlation effects in semiconducting SrTiO₃, *Phys. Rev. B* **81**, 235109 (2010).
- [113] W. Zhong and D. Vanderbilt, Competing Structural Instabilities in Cubic Perovskites, *Phys. Rev. Lett.* **74**, 2587 (1995).
- [114] R. F. Berger, C. J. Fennie, and J. B. Neaton, Band Gap and Edge Engineering via Ferroic Distortion and Anisotropic Strain: The Case of SrTiO₃, *Phys. Rev. Lett.* **107**, 146804 (2011).
- [115] J. H. Haeni, P. Irvin, W. Chang, R. Uecker, P. Reiche, Y. L. Li, S. Choudhury, W. Tian, M. E. Hawley, and B. Craigo, Room-temperature ferroelectricity in strained SrTiO₃, *Nature* **430**, 758 (2004).
- [116] T. F. Nova, A. S. Disa, M. Fechner, and A. Cavalleri, Metastable ferroelectricity in optically strained SrTiO₃, *Science* **364**, 1075 (2019).
- [117] A. Janotti, J. B. Varley, M. Choi, and C. G. Van de Walle, Vacancies and small polarons in SrTiO₃, *Phys. Rev. B* **90**, 085202 (2014).
- [118] X. Hao, Z. Wang, M. Schmid, U. Diebold, and C. Franchini, Coexistence of trapped and free excess electrons in SrTiO₃, *Phys. Rev. B* **91**, 085204 (2015).
- [119] E. Bousquet, M. Dawber, N. Stucki, C. Lichtensteiger, P. Hermet, S. Gariglio, J.-M. Triscone, and P. Ghosez, Improper ferroelectricity in perovskite oxide artificial superlattices, *Nature* **452**, 732 (2008).
- [120] M. Zacharias, M. Scheffler, and C. Carogno, Fully anharmonic nonperturbative theory of vibronically renormalized electronic band structures, *Phys. Rev. B* **102**, 045126 (2020).
- [121] Y. Aiura, I. Hase, H. Bando, T. Yasue, T. Saitoh, and D. S. Dessau, Photoemission study of the metallic state of lightly electron-doped SrTiO₃, *Surf. Sci.* **515**, 61 (2002).
- [122] S. A. Chambers, Y. Du, Z. Zhu, J. Wang, M. J. Wahila, L. F. J. Piper, A. Prakash, J. Yue, B. Jalan, S. R. Spurgeon, D. M. Kepaptsoglou, Q. M. Ramasse, and P. V. Sushko, Interconversion of intrinsic defects in SrTiO₃ (001), *Phys. Rev. B* **97**, 245204 (2018).
- [123] A. Fujimori, I. Hase, M. Nakamura, H. Namatame, Y. Fujishima, Y. Tokura, M. Abbate, F. M. F. de Groot, M. T. Czyzyk, J. C. Fuggle, O. Strebel, F. Lopez, M. Domke, and G. Kaindl, Doping-induced changes in the electronic structure of La_xSr_{1-x}TiO₃: Limitation of the one-electron rigid-band model and the Hubbard model, *Phys. Rev. B* **46**, 9841 (1992).
- [124] Y.-T. Chi, M. Youssef, L. Sun, K. J. Van Vliet, and B. Yildiz, Accessible switching of electronic defect type in SrTiO₃ via biaxial strain, *Phys. Rev. Mater.* **2**, 055801 (2018).
- [125] L. Rimai, J. L. Parsons, J. T. Hickmott, and T. Nakamura, Raman spectrum of long-wavelength phonons in tetragonal barium titanate, *Phys. Rev.* **168**, 623 (1968).
- [126] J. L. Parsons and L. Rimai, Raman spectrum of BaTiO₃, *Solid State Commun.* **5**, 423 (1967).
- [127] A. M. Quittet and M. Lambert, Temperature dependence of the Raman cross section and light absorption in cubic BaTiO₃, *Solid State Commun.* **12**, 1053 (1973).
- [128] F. Jona and G. Shirane, *Ferroelectric Crystals, International Series of Monographs on Solid State Physics* (Pergamon Press, Oxford, 1962).
- [129] H.-S. Lee, T. Mizoguchi, T. Yamamoto, S.-J. L. Kang, and Y. Ikuhara, First-principles calculation of defect energetics in cubic-BaTiO₃ and a comparison with SrTiO₃, *Acta Mater.* **55**, 6535 (2007).
- [130] Y. Xie, H. Yu, G. Zhang, and H. Fu, Lattice dynamics investigation of different transition behaviors of cubic BaTiO₃ and SrTiO₃ by first-principles calculations, *J. Phys. Condens. Matter* **20**, 215215 (2008).
- [131] V. Mishra, A. Sagdeo, V. Kumar, M. K. Warshi, H. M. Rai, S. K. Saxena, D. R. Roy, V. Mishra, R. Kumar, and P. R. Sagdeo, Electronic and optical properties of BaTiO₃ across tetragonal to cubic phase transition: An experimental and theoretical investigation, *J. Appl. Phys.* **122**, 065105 (2017).
- [132] A. M. Pugachev, V. I. Kovalevskii, N. V. Surovtsev, S. Kojima, S. A. Prosandeev, I. P. Raevski, and S. I. Raevskaya, Broken Local Symmetry in Paraelectric BaTiO₃ Proved by Second Harmonic Generation, *Phys. Rev. Lett.* **108**, 247601 (2012).
- [133] H. B. Gray, Molecular orbital theory for transition metal complexes, *J. Chem. Educ.* **41**, 2 (1964).
- [134] N. Tancogne-Dejean, F. G. Eich, and A. Rubio, Time-dependent magnons from first principles, *J. Chem. Theory Comput.* **16**, 1007 (2020).
- [135] P. Steneteg, B. Alling, and I. A. Abrikosov, Equation of state of paramagnetic CrN from *ab initio* molecular dynamics, *Phys. Rev. B* **85**, 144404 (2012).
- [136] F. Schmitt, P. S. Kirchmann, U. Bovensiepen, R. G. Moore, L. Rettig, M. Krenz, J.-H. Chu, N. Ru, L. Perfetti, and D. H. Lu, Transient electronic structure and melting of a charge density wave in TbTe₃, *Science* **321**, 1649 (2008).
- [137] G. Kresse and J. Furthmüller, Efficiency of *ab-initio* total energy calculations for metals and semiconductors using a plane-wave basis set, *Comput. Mater. Sci.* **6**, 15 (1996).
- [138] G. Kresse and J. Furthmüller, Efficient iterative schemes for *ab initio* total-energy calculations using a plane-wave basis set, *Phys. Rev. B* **54**, 11169 (1996).
- [139] J. Sun, A. Ruzsinszky, and J. P. Perdew, Strongly Constrained and Appropriately Normed Semilocal Density Functional, *Phys. Rev. Lett.* **115**, 036402 (2015).
- [140] C. Lane, J. W. Furness, I. G. Buda, Y. Zhang, R. S. Markiewicz, B. Barbiellini, J. Sun, and A. Bansil, Antiferromagnetic ground state of La₂CuO₄: A parameter-free *ab initio* description, *Phys. Rev. B* **98**, 125140 (2018).